2022

Power Decoupling Control and Optimization for a Photovoltaic Inverter in D-Q Rotation Frame

Zhaoxia Yang
Minnesota State University, Mankato

POWER DECOUPLING CONTROL AND OPTIMIZATION FOR A PHOTOVOLTAIC INVERTER IN D-Q ROTATION FRAME

by

Zhaoxia Yang

A THESIS

Presented to the Faculty of

The Graduate College at the Minnesota state

In Partial Fulfillment of Requirements

For the Degree of Master

Major: Electrical Engineering

Under the Supervision of Professor Qun Zhang

Minnesota State University, Mankato

March 2022

March 29, 2022

Power Decoupling Control and Optimization for a Photovoltaic Inverter in d-q Rotation Frame

Zhaoxia Yang

This thesis has been examined and approved by the following members of the student's committee.

_____

Professor Qun Zhang

Advisor

_____

Professor Vincent Winstead

Committee Member

_____

Professor Jianwu Zeng

Committee Member

POWER DECOUPLING CONTROL AND OPTIMIZATION FOR A PHOTOVOLTAIC INVERTER IN D-Q ROTATION FRAME

Zhaoxia Yang, M.S.

Minnesota State University, Mankato, 2022

Advisor: Qun Zhang

In the past decade, solar energy, the fastest growing renewable energy, has been a growing interest in integration to the utility grid. Power electronics converters play important role in renewable energy integration, e.g., integrate the distributed photovoltaic (PV) panels to the grid. In many applications, particularly in the residential area, a single-phase rather than three-phase inverter is used to regulate the voltage from one form to the other while tracking the maximum power point of the PV system.

The input voltage and current are DC and its maximum power is desired to be a constant value. However, in the single-phase PV inverter, the sinusoidal voltage and current waveform makes the output power pulsated with double frequency, which results in the power mismatch between the input and the output. Therefore, it is necessary to use energy buffer to balance the power, i.e., the power decoupling.

In this work, a power decoupling method first is developed in d-q rotation frame and is optimized so that the energy buffer can be minimized. The power decoupling controller designed in the d-q frame has the superiority of simplicity so that the traditional proportional integral (PI) control can be used. Besides, a composite power decoupling method which includes both DC side passive and AC side active power

decoupling is developed. Due to the use of two stage power decoupling, the energy buffer, e.g., capacitance at the DC and AC side, is minimized. Meanwhile, the important functions such as the maximum power point tracking (MPPT) and relatively high power quality are achieved.

ACKNOWLEDGMENTS

I am very cherishing this chance of study at Minnesota State University, Mankato. From the bottom of my heart, I would like to say big thanks to the people who have guided and helped me during my graduate school life.

First, I wish to express my sincere appreciation to my supervisor, Qun Zhang, who have encouraged me often, helped me from both academic and life, and led me to the depth of academic research. His meticulous and rigorous scholarship enthusiastic work attitude benefits me a lot.

In addition, I wish to say thanks to my thesis committee members Dr. Vincent Winstead and Dr. Jianwu Zeng for their advice and comments on my thesis research. Simultaneously, I wish to say thank you to the department of Electrical and Computer Engineering and Technology (ECET) for its provided resource, support and considerate guidance of the faculty and staff.

What's more, I am very grateful to my family and my friends for their continuously love and unconditional support. At the same time, I am very appreciating to all the research group members in the labs. Their accompany made my graduate life more colorful, energetic, convenience and warm.

At last, the financial support from the Xcel Energy through a grant from the Renewable Development Fund is gratefully acknowledged.

TABLE OF CONTENTS

Chapter 1 : Introduction

1.1 Background

Due to the growth demand of global energy and adverse effects of conventional energy such as pollution caused by fossil fuel and nuclear fission sources, the exploration of the renewable energy sources (RES) is increased [1]. Renewable energy, as clean and alternative energy, is based on self-renewing energy sources including the solar energy, wind energy, wave energy, tidal energy, ocean thermal energy, hydropower, the geothermal energy, and biomass energy [2]-[4]. With increasing concern about the environmental issues, RES are paid more and more attention. The growth rate of renewable power installation has exceeded that of the fossil fuel and nuclear power capacity combined [5]-[8]. For example, in 2021, the installed renewable power capacity is increased more than 290 GW, mostly are PV which has the largest growth rate ever and enhanced the global total to 2,588 GW by the end of year [8]. The Renewables Market Report said growth will accelerate to average 305 GW per year for 2021 through 2026. By the end of 2026, global renewables capacity will reach 4,800 GW, or 60% greater than at end 2020. Renewables will represent about 95% of the new power capacity installed worldwide from now through 2026 [9].

Since the electricity generated from RES is more cost effective than that from the coal-fired power plants [2], it is cheaper to build new wind or PV plants than utilizing existing coal-fired power plants [3]. Besides, renewables also beat new natural gas power

station on cost in many locations and has become the cheapest sources of new electricity generation on the earth (excluding Antarctica [4]).

Among the clean energy technologies, PV has significantly grown in recent years [6],[8]. Not only the efficiencies of the most domestic solar panels are low, i.e., around 10-20%, but the performance of other components such as inverters and batteries are limited as well. Battery, which can provide fast response for balancing the power between the generation and consumption [11], is becoming a good candidate for the electrical energy storage system (ESS). However, the initial installation costs are still high [12].

Power electronic converters, which regulate voltages from one form to another are compatible with end-use electricity supply, are key elements for renewable energy power generation . Inverters that convert DC to AC voltages is broadly used in solar power conversion. In some applications such as the residence area, a single-phase PV inverter is usually used.

1.2 Solar Energy System

Solar energy is harvested with technologies such as PV, solar heating and cooling, solar thermal, and solar architecture [13]. In this thesis, we will focus on PV system. In this system, the electricity is first generated by the PV panel and then the inverter is used to regulate the DC voltage to AC voltage.

1.2.1 PV System

Solar energy is harvested with technologies such as PV, solar heating and cooling, solar thermal, solar architecture [13]. Figure 1.1 shows the overview of PV system integration to the utility grid, the PV panels first are connected in parallel and in series, then a DC-AC inverter is used to regulate the voltage from DC to AC. The inverters are connected to the distribution line which has a low voltage bus. As shown in the Figure 1.1, once the electricity is generated by the PV panel, inverter is used for solar energy conversion. Therefore, the PV inverters play important role in solar energy integration. It not only converts the voltage forms, i.e., from DC PV voltage to AC voltage with fixed 60 Hz frequency, but also can harvest the solar power from as much as possible.

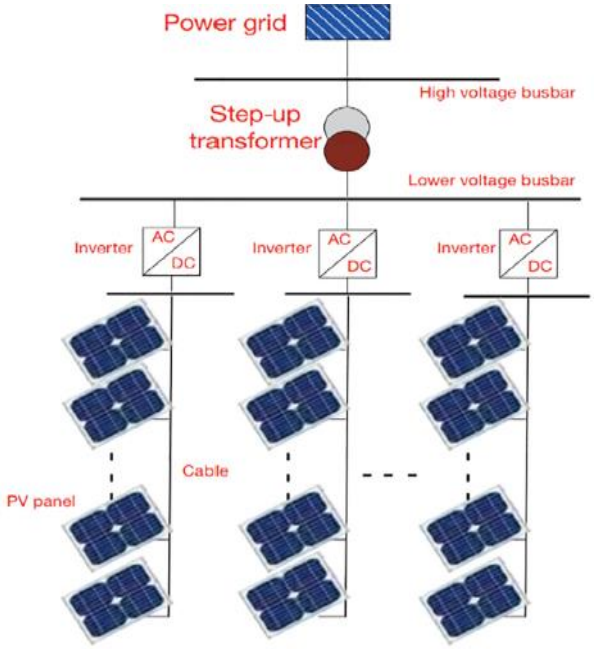

Figure 1.1: An overview of solar power (PV systems) integration into electricity.

Unlike the conventional voltage source in which power is proportional to the current, it is well-known that a PV panel has nonlinear characteristics, e.g., current vs. voltage (I-V).

1.2.2 PV Characteristic Curves

These nonlinear characteristics is modeled with the use of the equivalent circuit of the PV panel as shown in Figure 1.2.

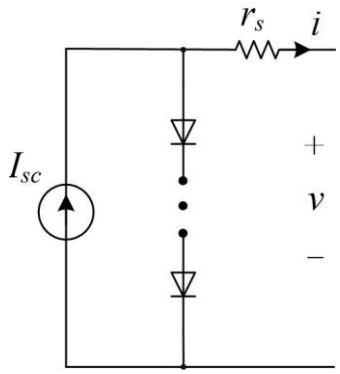

Figure 1.2: The equivalent circuit of the PV panel.

The relationship between the current and voltage of the PV panel can be expressed as follows.

$$i = I_{sc} - I_s \cdot \left[e^{\frac{q\cdot(v+i\cdot r_s)}{k\cdot T}} - 1 \right] \tag{1.1}$$

where I_{sc} is the short circuit current of the PV panel; I_s is the reverse saturation current; v and i are is the terminal voltage and current of the PV panel, respectively; r_s is the PV panel series resistance; q (= 1.6×10^{-19}) is an electron charge; T is the operating

temperature; and k (= 1.38×10^{-23} J/K) is the Boltzmann constant. The short circuit current depends on the solar radiation and temperature.

Figure 1.3 shows the characteristic curves of solar panel. As shown in Figure 1.3 (a), when the voltage is low, the current is relatively constant, the PV panel works as a constant current source; when the voltage approaches its open circuit voltage, the PV panel can be treated as a constant voltage source.

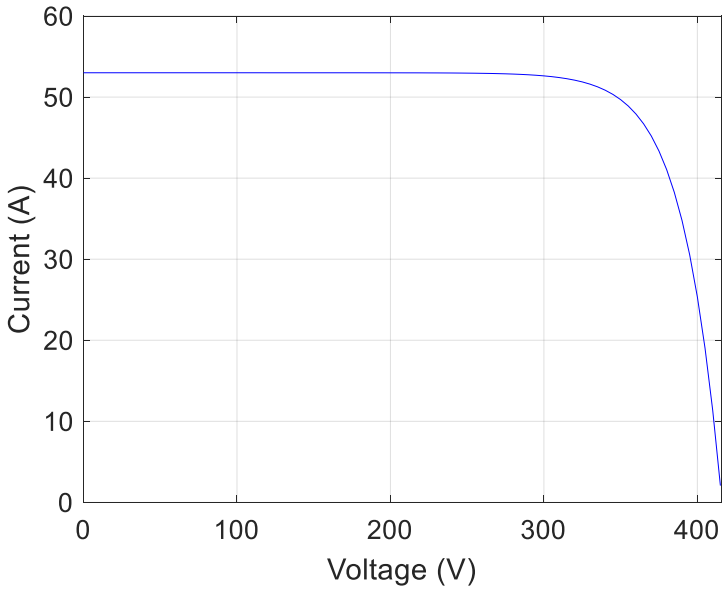

(a)

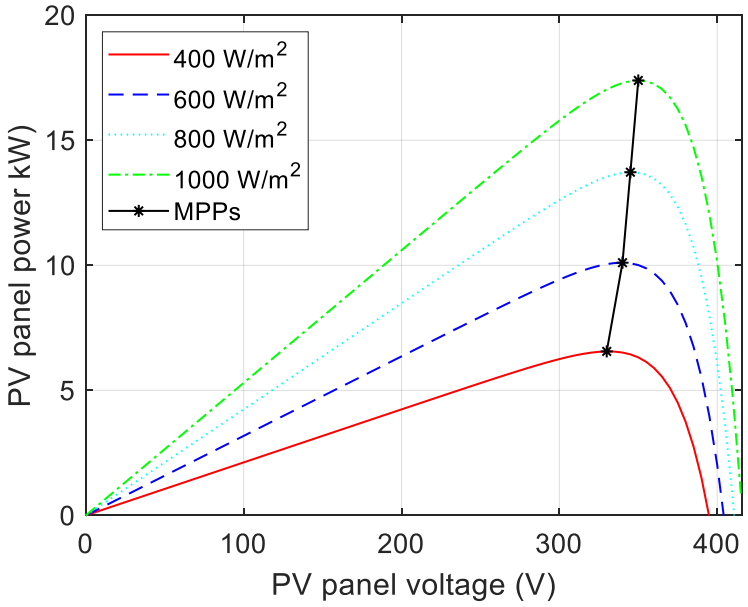

(b)

Figure 1.3: Characteristic curve of the PV panel. (a) I-V curve; (b) P-V curve.

When the solar radiation is changed from 400 W/m^2 to 1000 W/m^2. As shown in Figure 1.3(b), the stronger the radiation is, the larger power becomes. When the voltage is low, the power is proportional to the voltage. The power is first increased and decreased with the voltage, therefore, for a given solar radiation, there is a unique maximum power point (MPP), which can be achieved by setting its corresponding voltage to V_{mpp}. With the change of the solar radiation, both the MPP and its corresponding voltage change. It is necessary to tracking its MPPs all the time to extract power from the PV panel as much as possible, namely MPPT control.

1.2.3 MPPT Control

Existing MPPT algorithms include perturbation and observation (P&O), constant voltage, incremental conductance, and computational intelligence-based algorithms. Among these methods, P&O and incremental conductance algorithms are commonly used in a variety of applications due to their simplicity. In this thesis, the P&O algorithm which is shown in Figure 1.4 is selected for MPPT control of PV systems. For a given perturbation voltage ΔV, the power variation ΔP is calculated, then the next voltage is updated as follows:

$$\Delta V_{k+1} = sign\left(\Delta V_k \cdot \Delta P_k\right) \tag{1.2}$$

where sign(·) represents the sign function.

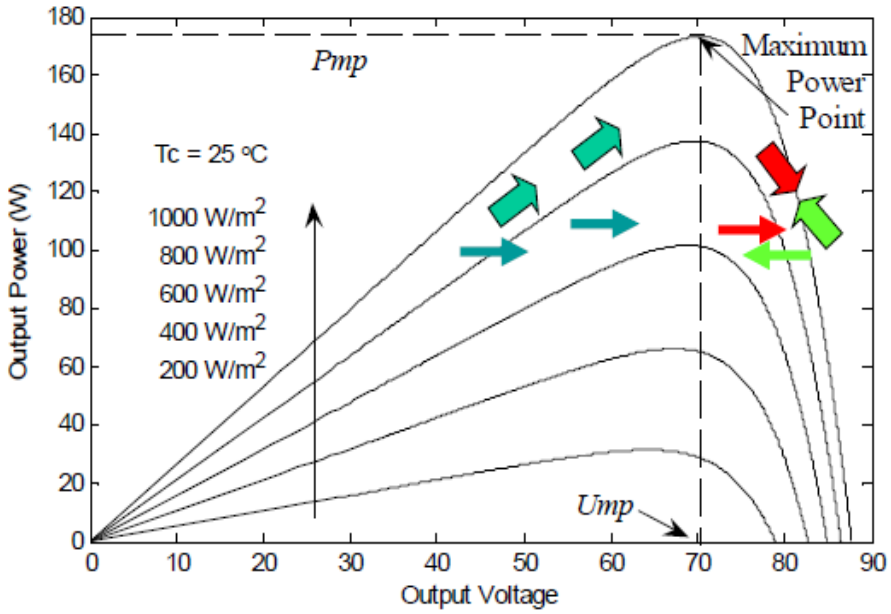

Figure 1.4: P&O MPPT algorithm.

1.3 PV Inverter and Power Decoupling

As shown in Figure 1.1, the PV inverter is usually used for PV system integration. On one hand, it regulates the DC voltage to AC, on the other hand, the maximum solar power is delivered to the grid. Figure 1.5 shows the voltage, current, and power waveforms in PV panel and inverter.

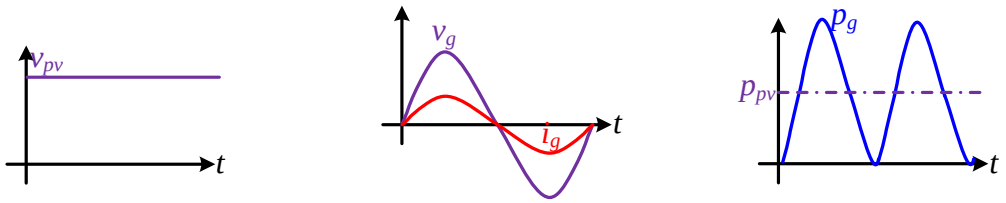

(a) (b) (c)

Figure 1.5: Voltage and power waveforms. (a) PV voltage; (b) inverter output voltage and current; (c) power of inverter and PV panel.

As shown in Figure 1.5, the input PV voltage is a constant value, the output voltage and current of the inverter is sinusoidal waveform with 60 Hz. Then the power of the PV panel (p_{pv}) is constant DC and the output power (p_g) pulsated with 120 Hz. Since the power needs to be balanced anytime, it is necessary to use the energy storage device remove the pulsated power, i.e., when the input solar power is larger than the output power, the surplus power is absorbed; when the solar power is less than the output, the energy storage device provides the deficient power. Therefore, the 120 Hz ripple power is removed. The focus of this thesis is to design and control PV inverter to achieve the power decoupling.

1.4 Outline of Thesis

This thesis will be organized as follows.

Chapter 2 reviews the existing power decoupling methods, including the conventionally used passive power decoupling, active power decoupling, and hybrid power decoupling methods.

Chapter 3 modeling and design control in the d-q rotation frame, the designed controllers in the d-q frame reduce the complexity so that the traditional proportional integral (PI) controller can be used.

Chapter 4 optimizes the power decoupling circuit by dynamically allocating the passive and active power decoupling method. The voltage ripple and the capacitance used in the inverter is minimized.

Finally, the thesis ends with conclusions, a summary of contributions, and recommendations for future work in Chapter 5.

Chapter 2 : Power Decoupling Methods

For those applications power rating is lower than 10 kW, e.g., residential PV system, the single-phase conversion is commonly used [14]. During the integration of these distributed PV arrays to the power system, single-phase inverters play an important role in the energy conversion as well as voltage regulation. However, due to the double-line-frequency issue of the single-phase inverter, i.e., there is voltage/current ripple generated at the dc-link [14],[15]. Such voltage ripple degrades system performance such as the maximum power point tracking (MPPT) efficiency of the PV system [15].

Taking the view of the issue from the perspective of power. The instantaneous power of the single-phase inverter can be expressed as follows:

$$\begin{aligned} p(t) &= v_g \cdot i_g = \sqrt{2} \cdot V_g \sin(\omega t) \cdot \sqrt{2} \cdot I_g \sin(\omega t - \varphi) \\ &= \underbrace{S \cdot \cos\varphi}_{P} - \underbrace{S \cdot \cos(2\omega t - \varphi)}_{\tilde{p}} \end{aligned} \tag{2.1}$$

where S and $\tilde{P}$ represents the apparent power and AC component (or pulsating power component) of the instantaneous power, respectively; V_g and I_g are the root mean square (RMS) values of v_g and i_g on the AC side, φ is the phase angle difference between v_g and i_g.

Equation (2.1) shows that p is composed of a constant component (P) and an oscillation component ($\tilde{P}$) at double load/grid frequency. Therefore, the output power of the inverter is pulsated with double line frequency. However, the input solar power is desired to be constant. Figure 2.1 shows the output power of the inverter and the input

solar power. The pulsating power is transferred to the dc side, which generates a second-order ripple on the dc voltage/current. The undesirable ripple results from power mismatch. Therefore, extra energy storage system (ESS) is required to be placed between the PV and output of the inverter to eliminate the pulsating power, which is also called power decoupling [16]-[18]. For example, when $p_o > p_{pv}$, EES provides the deficient power; otherwise, ESS stores the surplus power. Then the solar power can be harvested as much as possible.

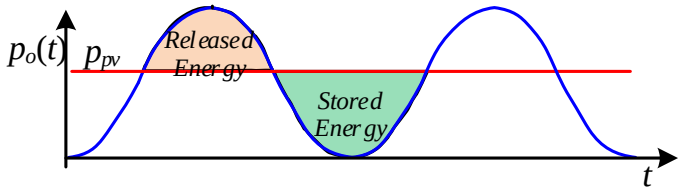

Figure 2.1. Power decoupling of the PV system with the ESS.

The power decoupling technology can be generally divided into control and topology parts, which means that modification of the control strategy or the topology with additional components can eliminate (or suppress) the double frequency ripple [19]. Then the power decoupling method can be classified as passive power decoupling method, active decoupling method and hybrid power decoupling method.

2.1 Passive Power Decoupling Method

The conventional passive solutions are usually using a capacitor or LC filter on the PV side or inverter dc-link to absorb the ripple power. This solution is simple and easy to be implemented because it does not need extra control and hardware [20][21].

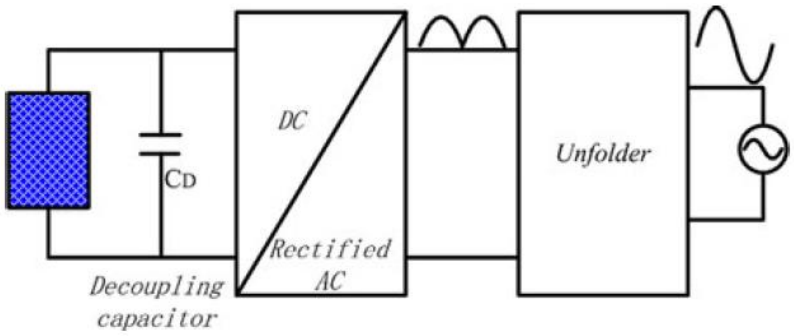

Figure 2.2. Passive power decoupling for single stage inverter [14].

As shown in Figure 2.2, only the decoupling capacitor C_D is installed at the PV side. C_D with large capacitance is needed if power is decoupled on the PV side only to keep Δv_{dc} to very low value for achieving high MPP efficiency [22]. For example, regarding a 200-W microinverter to realize a 98% PV utilization factor, the required minimum decoupling capacitance is 13.9 mF [14]. This represents a very large value. Due to the requirement of high capacitance, usually an aluminum electrolytic capacitor is used. Electrolytic capacitors typically have a limited lifetime, namely 1000~7000 hours at 105^{o}C operating temperature [23]. Additionally, the electrolytic capacitors are usually oversized. Therefore, the bulky electrolytic capacitor not only increases the size of the microinverter but also reduce the lifetime of the inverter. In short, using electrolytic capacitor alone is far from being a satisfying solution to power decoupling [24].

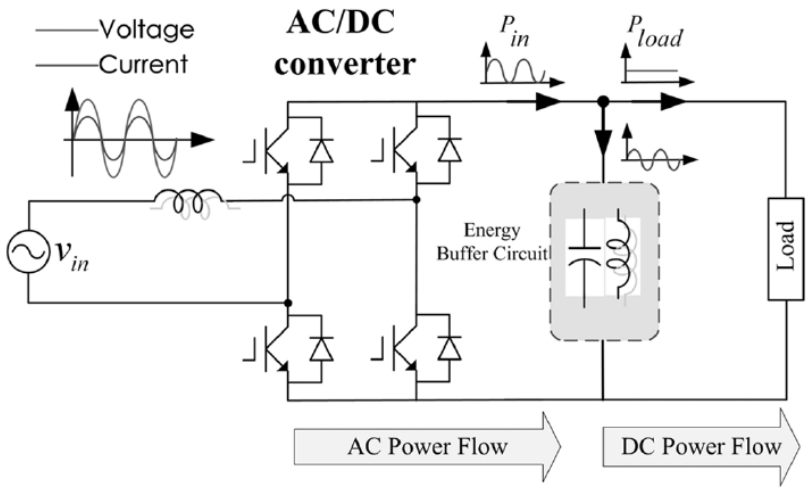

Figure 2.3 Single-phase ac–dc converter with conventional power decoupling [24].

Figure 2.3 shows LC power decoupling for a single-phase ac-dc converter. The LC resonance filter can suppress the DC-side ripple for sharing certain current with the DC side. However, the resonance frequency is very low (e.g.,120 Hz for a 60-Hz grid), the weight and size of the passive components are comparatively large, so we need to consider them. Additionally, the voltage across the capacitor of the LC filter can be much higher than the maximum dc-link voltage [25].

2.2 Active Power Decoupling Method

To resolve the drawback of the passive power decoupling solutions, active decoupling methods are created. Therefore, the basic idea of active decoupling method is the use of a new specific energy storage device with relatively small size and long lifetime to instead the original passive components. It is realized through the addition of active switching devices (such as diodes, transistors), and filters [26]-[32].

This kind of decoupling method usually involves a lot of additional power semiconductor devices, which increases cost significantly.

According to the connection way of the active decoupling circuit with DC side, they are divided into series compensation (decoupling circuit in series with PV), parallel compensation (decoupling circuit in parallel with PV) [14][15][27]. Figure 2.4 shows the schematic of parallel mode and series mode.

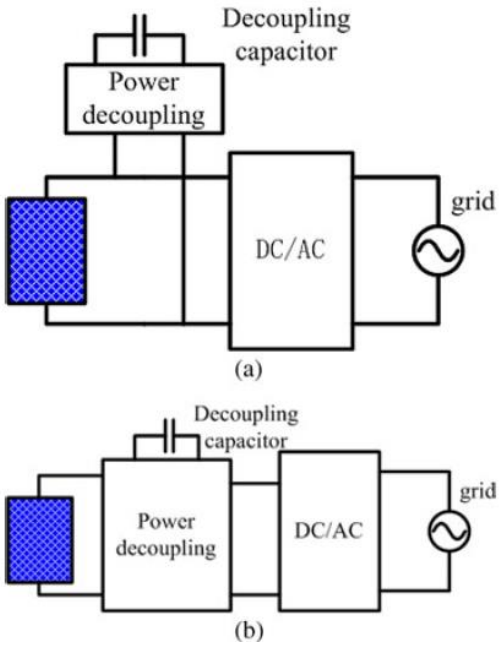

Figure 2.4 Different ways of connection for power decoupling.

(a) Parallel mode; (b) Series mode [14].

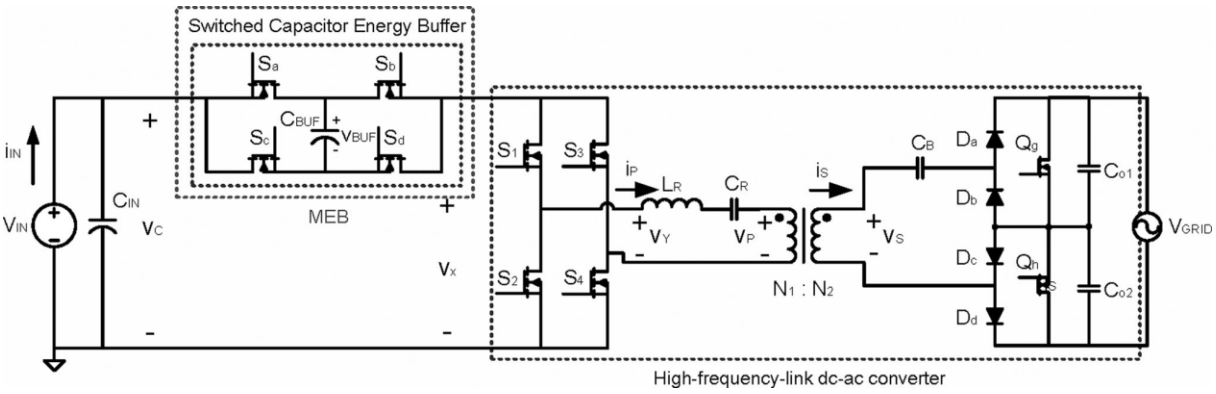

Figure 2.5 Schematic of a microinverter without the charge control circuit (CCC) [28].

Figure 2.5 shows the schematic of a simplified multilevel energy buffer and voltage modulator (MEB) microinverter without the CCC. The switched-capacitor energy buffers (SCEB) are connected in series between the PV side and converter. The SCEB is composed of four switches and one buffer capacitor C_{BUF}. Assume that the C_{BUF} is so large that v_{BUF} does not vary much during a line cycle. Therefore, C_{BUF} is an active energy buffer to reduce the double-line-frequency ripple. Since C_{BUF} is not across the PV panel, the voltage ripple across it can be larger than that the buffer capacitor is across the PV side. And in the MEB microinverter, the double-line-frequency ripple is decoupled by both C_{IN} and C_{BUF}. Therefore, the energy storage C_{IN} and its size can be reduced to a smaller level in this way [28].

There are some other series connection topologies in literature [29],[30]. Figure 2.6 is another example of series connection [29]. The active buffer circuit lies between the converter and DC side. Because the active buffer circuits are connected in series, the

PV power is transferred to the end through active buffer filter. Then the efficiency of the whole system may decrease certain amount. Additionally, the active buffer filter partly depends on original topology.

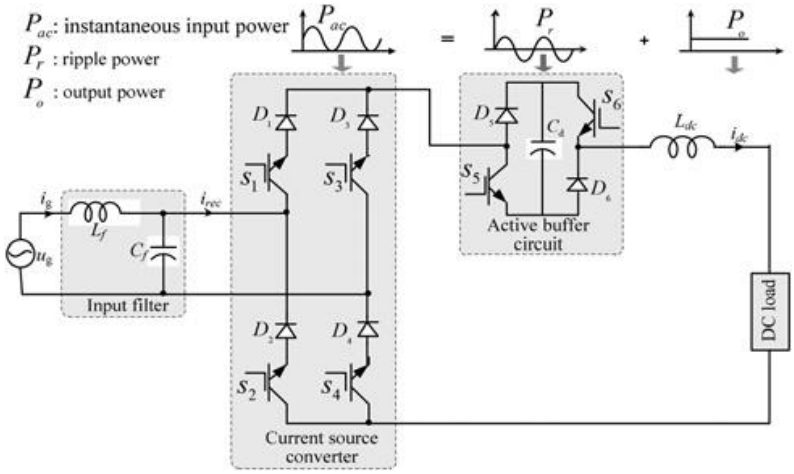

Figure 2.6 Proposed converter topology in [29].

The parallel connection topology of the active power decoupling method is commonly used [27],[28] [32]-[35].

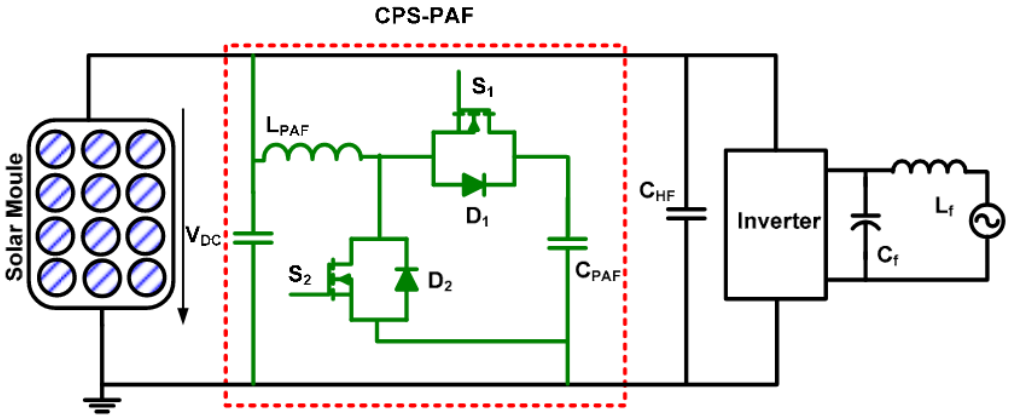

Figure 2.7 The Current Pulsation Smoothing Parallel Active Filter in [32].

As shown in Figure 2.7, the enclosed range with red dash line is the part of the current pulsation smoothing parallel active filter (CPS-PAF). Since it is connected in parallel, not all the PV power is flowing through the CPS-PAF. Then the system efficiency decrease from CPS-PAF is smaller than that from the series connected active filter. The PV module can be operated close enough to the maximum power point.

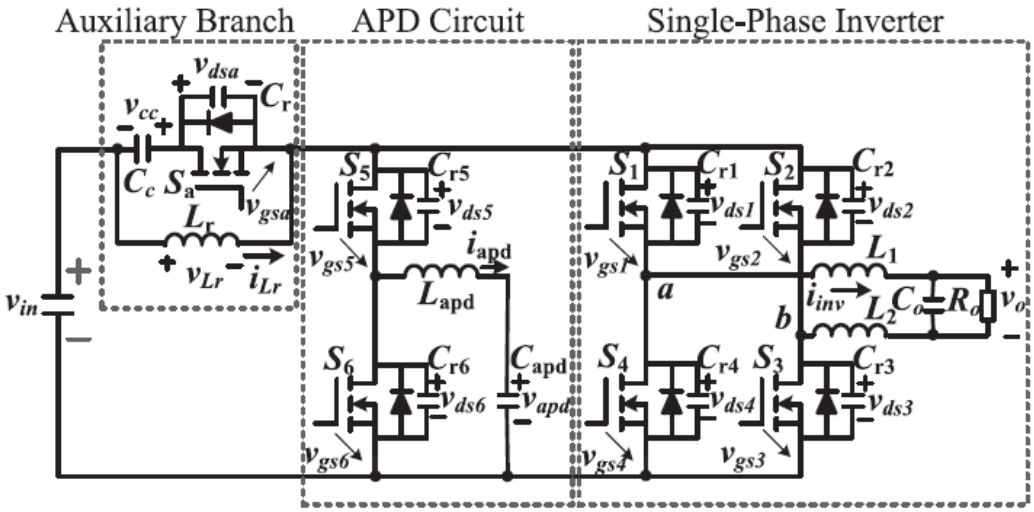

Figure 2.8 Topology for an inverter with active power decoupling [34].

Figure 2.8 shows the zero-voltage-switching (ZVS) topology of single-phase full-bridge inverter with buck-type APD. The APD is connected in parallel with the inverter. The dc bus current ripple is reduced dramatically by adding the APD to the topology [34].

Although the research about active power decoupling is in in full swing, some preliminary conclusions are drawn. First, most of the active decoupling filters are connected in parallel with the main inverter. One reason is that higher system efficiency can be obtained easily in the parallel-connected topology. Because only the ripple energy

is processed in the parallel-connected active ripple filter and all the main power are processed in the series-connected mode, there are more loss in the series-connected mode [19][32]. Another reason is that control methods and modulation strategies are more flexible in the parallel-connected topology since the active filter is independent from the inverter [32]. Second, the capacitors are used in most of the active power decoupling method [14]. This is based on the inductor is found not to be as good as the capacitor in terms of energy density for an application using a few hundred hertz, which means the captive device is more effective at having smaller energy storage component volume [35]. There are two major reasons for this. For one thing, a larger magnetic core size is required to meet the flux saturation requirement for the inductor, this is because the magnetic material saturation flux will limit the inductor's volume; for another thing, more volume is required for inductor's thermal dissipation to meet the temperature rise requirement, because of the more energy loss of inductor compared with that of the capacitor [35]-[36].

The reason is higher energy density can be achieved in capacitor compared with inductor. With certain requirements of energy storage and the operating frequency, energy storage components size is reduced for both inductive and capacitive method.

2.3 Hybrid Method

The addition of active switching devices is the typical character of active power decoupling. However, this will lead to the cost increase significantly. Most researchers

paid more attention to the active power decoupling topologies with the features of low cost, low volume and weight, high efficiency, high reliability, and high performance. Recently, some topology without any additional semiconductors has developed. A structure of a single-phase H-bridge voltage source converter (VSC) shown in Figure 2.9 is proposed in [20]. Only two capacitors are required to place between the midpoint and one end of each inverter leg to decouple the ripple power. The design is simple, and the ripple power is transferred toward the capacitors.

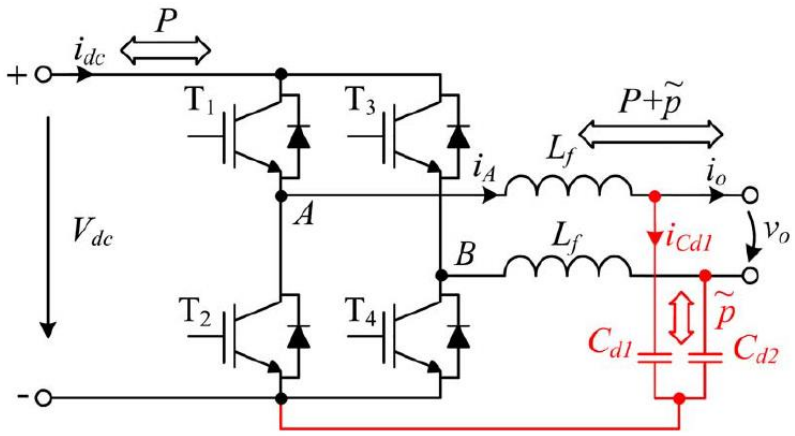

Figure 2.9 Structure of the single-phase VSC with decoupling circuit [20].

However, in this way, switches multiplexing is usually the choice, which will result in the system suffer from more constraints, such as increasing voltage/current stress, reduced operation range, increased volume, and complicated control algorithms [15]. On the other hand, the power decoupling topologies with switch multiplexing benefit from fewer power semiconductor devices. However, they usually suffer from more constraints, such as voltage/current stress increase, reduced operation range, increased volume, and complicated control algorithms [20].

Recently, Single-phase power decoupling technique utilizing hybrid method with passive and active power decoupling is proposed in [37] [see Figure 2.10]. From Figure 2.10 (b), we can see that power decoupling circuit consists of the boost type DC active filter and passive capacitor (C_{dc}) together. According to the authors, the power density of the hybrid method is higher in comparison with the active power decoupling operation and the passive method.

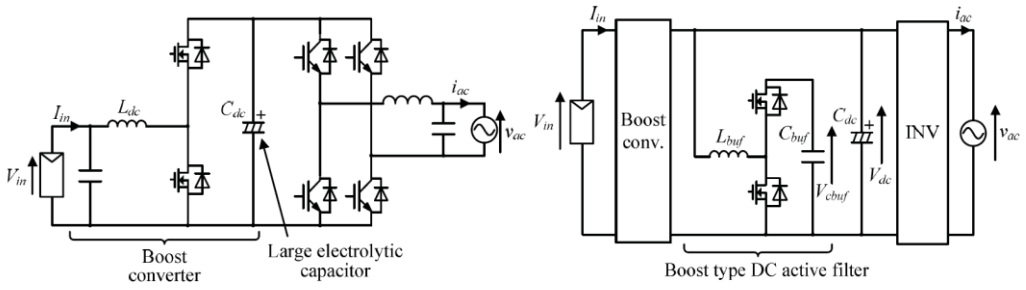

(a) (b)

Figure 2.10 Circuit configuration: (a) original single-phase inverter;(b) boost type DC active filter [37].

2.4 Summary

This chapter is mainly about the power decoupling methods from the view of connection ways. Then three different decoupling method, passive decoupling method, active decoupling method and hybrid method are described respectively. In fact, the principle of the hybrid method is the addition of the passive and active power decoupling methods.

Chapter 3 : Two-Stage Power Decoupling Power Decoupling in D-Q Frame

Recently, a power decoupling method without using additional power electronics devices is introduced [20]. However, the use of parameter dependent proportional resonant (PR) controllers may not achieve satisfactory compensation in case there are parameter drifts in the system [38]-[44]. Furthermore, the existing power decoupling methods are achieved either on DC side or AC side [14], [20], [24], [47],[48], the traditional PI controller cannot be used due to the need of the large gain at the grid frequency or double grid frequency. The power decoupling control in D-Q frame has superiority of dealing with the DC-link voltage ripple [49].

This chapter presents modeling and designing controllers for a PV inverter by controlling the DC-link voltage ripples in the D-Q frame. The proposed power decoupling will be achieved on both DC and the AC side with all film capacitors, which increases the overall reliability of the converter. Besides, in the D-Q frame, the conventional proportional integral (PI) controllers can be easily designed and used for power decoupling.

3.1 Principle of Two-Stage Power Decoupling

As we mentioned before, equation (2.1) shows that the instantaneous power of the converter is composed of a continuous component (P) and an oscillation component ($\tilde{P}$)

at twice the load/grid frequency. This chapter is to model and design controllers of an inverter with smaller capacitance to achieve power decoupling on both DC and AC sides.

The amount of decoupling power on the DC side can be calculated as follows:

$$p_{dc} = 2 \cdot \omega \cdot C_{dc} \cdot V_{dc} \cdot \Delta v_{dc} \tag{3.1}$$

where ω is the angular frequency of the grid; V_{dc} and Δv_{dc} are the DC and AC components of v_{dc}, respectively. As indicated in equation (3.1), a large value of C_{dc} is needed if power is decoupled on the DC side only. Such large capacitance requires to use an electrolytic capacitor which has lower reliability than the film capacitor.

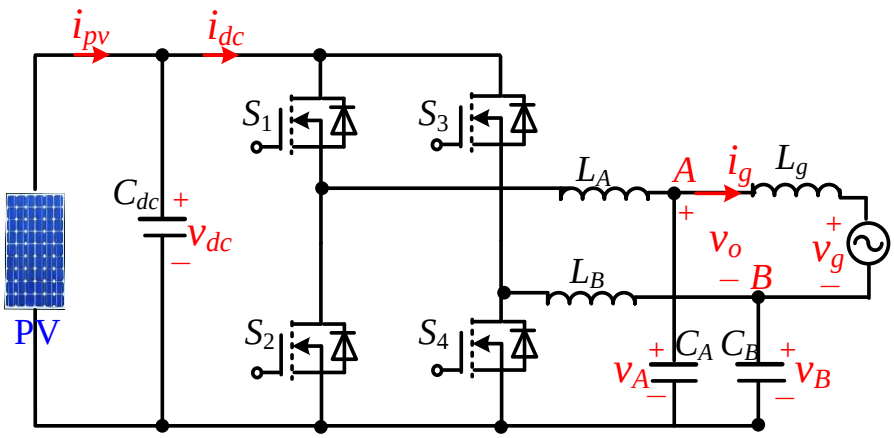

Figure 3.1 Two-stage power decoupling PV inverter.

On the AC side, to remove the pulsating power with small capacitance, two capacitors, C_A and C_B are added on a H-bridge inverter as shown in Figure 3.1. On one hand, the voltage difference between v_A and v_B is controlled to be v_g; on the other hand, two capacitors C_A and C_B are used for absorbing the pulsating power component on the AC side. For simplicity purposes, the voltage drop on the inductors L_A and L_B will be neglected in the analysis for the calculation of the voltage of the C_A and C_B [20]. Then

the pulsating power on the AC side is decoupled by the capacitors C_A and C_B. Since v_o is sinusoidal waveform, v_{AB} can be solved as follows:

$$v_{AB} = \sqrt{\frac{P_{ac} \cdot \sin(2\omega t)}{2\omega \cdot C_2} + V_{c0}^2 - \frac{v_o^2}{4}} \pm \frac{v_o}{2} \tag{3.2}$$

where P_{ac} represents the power decoupled on the AC side; V_{c0} is the initial voltage of C_A and C_B; $C_A = C_B = C_2$.

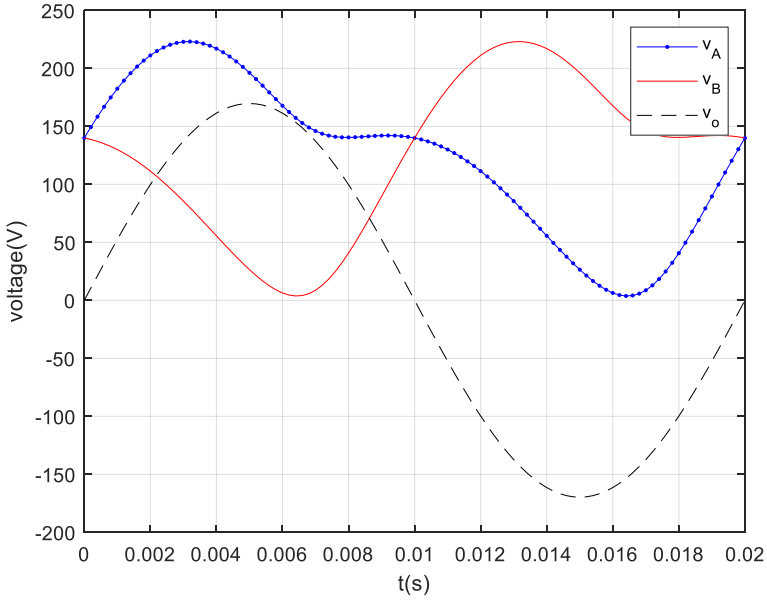

Figure 3.2 Ideal waveforms of the inverter.

Figure 3.2 shows the ideal waveforms of v_A, v_B, and v_o, as shown in Figure 3.2, v_A and v_B are DC voltages while its difference v_o is AC voltage with sinusoidal waveform.

3.2 Modeling and Controllers Design

There are three objectives of this PV inverter: 1) to regulate the output current v_g to be sinusoidal waveform; 2) to achieve the MPPT for the PV panel; 3) to realize power

decoupling on both DC and AC side such that all film capacitor with small capacitance can be used.

3.2.1 State-space Equation

In this chapter, $L_A = L_B = L_2$, with the average state-space method, the average model of the whole PV inverter can be derived as follows:

$$\begin{cases} C_{dc} \cdot \dfrac{dv_{dc}}{dt} = i_{pv} - i_A \cdot d_A - i_B \cdot d_B \\ C_2 \cdot \dfrac{dv_A}{dt} = i_A - i_g \\ L_2 \cdot \dfrac{di_A}{dt} = v_{dc} \cdot d_A - i_A \cdot r_2 - v_A \\ C_2 \cdot \dfrac{dv_B}{dt} = i_B + i_g \\ L_2 \cdot \dfrac{di_B}{dt} = v_{dc} \cdot d_B - i_B \cdot r_2 - v_B \\ L_g \cdot \dfrac{di_g}{dt} = v_A - v_B - r_g \cdot i_g - v_g \end{cases} \tag{3.3}$$

where r_2 and r_g are the parasitic resistors of L_2 and L_g, respectively; d_A, and d_B are the duty cycles of S_1 and S_3, respectively. The model described in equation (3.3) is a multi-input multi-output system. By introducing the common and differential mode signals into equation (3.3), e.g., $i_c = i_A + i_B$; $i_d = i_A - i_B$; $v_c = v_A + v_B$, $v_d = v_o = v_A - v_B$, $D = (d_A + d_B)/2 = v_{com}/V_{dc}$, $d = (d_A - d_B)/2 = v_o/(2V_{dc})$, then equation (3.3) can be rewritten as:

$$\begin{cases} v_d = L_2 \dfrac{di_d}{dt} + v_o + i_d \cdot r_2 \\ i_d = c_2 \dfrac{dv_o}{dt} + 2i_g \\ v_o = v_g + L_g \dfrac{di_g}{dt} + r_g \cdot i_g \end{cases} \tag{3.4}$$

$$\begin{cases} L_2 \cdot \dfrac{di_c}{dt} = -i_c \cdot r_2 - v_c + 2v_{com} \\ C_2 \cdot \dfrac{dv_c}{dt} = i_c \\ C_{dc} \cdot \dfrac{dv_{dc}}{dt} = i_{pv} - \dfrac{2v_{com}}{V_{dc}} \cdot i_c - \dfrac{2v_d}{V_{dc}} \cdot i_d \end{cases} \tag{3.5}$$

When PV panel works in the vicinity of the maximum power point (MPP), the first derivative of its power with respect to its voltage is zero.

$$dp_{pv} = I_{mpp} \cdot v_{pv} + V_{mpp} \cdot i_{pv} = 0 \tag{3.6}$$

where V_{mpp} and I_{mpp} represent the voltage and current of the PV panel when it works at MPP, respectively [46]. Then

$$i_{pv} = -\frac{I_{pv}}{V_{mpp}} \cdot v_{dc} = \frac{-1}{r_{pv}} \cdot v_{dc} \tag{3.7}$$

where r_{pv} represents the equivalent resistance of the PV panel around the MPP. Then equation (3.7) can be further written as:

$$\begin{cases} L_2 \cdot \dfrac{di_c}{dt} = -i_c \cdot r_2 - v_c + 2v_{com} \\ C_2 \cdot \dfrac{dv_c}{dt} = i_c \\ C_{dc} \cdot \dfrac{dv_{dc}}{dt} = \dfrac{-1}{r_{pv}} \cdot v_{dc} - \dfrac{2v_{com}}{V_{dc}} \cdot i_c - \dfrac{2v_d}{V_{dc}} \cdot i_d \end{cases} \tag{3.8}$$

The differential equations of the differential and common signals in the *α-β* stationary frame can be found as follows:

$$\underbrace{L_2 \cdot L_g \cdot C_2}_{a_{i3}} \cdot \dddot{i}_g^{(\alpha\beta)} + \underbrace{\left(L_2 \cdot r_g \cdot C_2 + L_g \cdot r_2 \cdot C_2\right)}_{a_{i2}} \cdot \ddot{i}_g^{(\alpha\beta)} + \underbrace{\left(r_g \cdot r_2 \cdot C_2 + L_g + 2L_2\right)}_{a_{i1}} \cdot \dot{i}_g^{(\alpha\beta)} + \underbrace{\left(r_g + 2r_2\right) i_g^{(\alpha\beta)}}_{a_{i0}} = v_d^{(\alpha\beta)} \tag{3.9}$$

$$\begin{aligned} &\dddot{v}_{dc}^{(\alpha\beta)} + \underbrace{\left(\frac{r_2}{L_2} + \frac{1}{r_{pv} \cdot C_{dc}}\right)}_{a_{v2}} \cdot \ddot{v}_{dc}^{(\alpha\beta)} + \underbrace{\frac{1}{L_2 \cdot C_{dc}} \cdot \left(\frac{r_2}{r_{pv}} + \frac{C_{dc}}{C_2} + \frac{1}{2}\right)}_{a_{v1}} \cdot \dot{v}_{dc}^{(\alpha\beta)} + \underbrace{\frac{1}{L_2 \cdot C_2 \cdot r_{pv} \cdot C_{dc}}}_{a_{v0}} v_{dc}^{(\alpha\beta)} \\ &+ \underbrace{\frac{V_{dc} \cdot I_c}{C_{dc}}}_{b_{v2}} \ddot{v}_{com}^{(\alpha\beta)} + \underbrace{\frac{V_{dc}}{L_2 \cdot C_{dc}} \cdot \left(I_c \cdot r_2 + V_{dc}\right)}_{b_{v1}} \dot{v}_{com}^{(\alpha\beta)} + \underbrace{\frac{V_{dc} \cdot I_c}{C_{dc} \cdot L_2 \cdot C_2}}_{b_{v0}} v_{com}^{(\alpha\beta)} = 0 \end{aligned} \tag{3.10}$$

3.2.2 d-q Transformation

The main function of the d-q transformation is to change the variables from a stationary to a rotating frame. Hence the time-varying variables such as current components and voltage components become DC in d-q frame instead of AC values in stationary frame [50]-[52]. Therefore, the control method for the single-phase converters with zero steady state error can be implemented. The d-q transformation is originally used in three-phase synchronous machine [50].

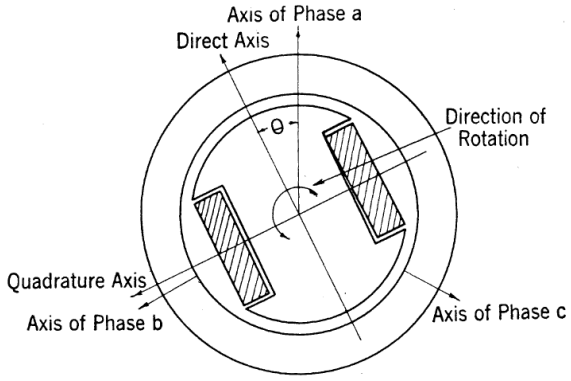

Figure 3.3 the schemtaic of ideal symmetrical three-phase synchronous machine [50].

For the three-phase system, as shown in Figure 3.3, in a-b-c coordinates, axis of phase a, axis of phase b and axis of phase are fixed on the same plane, apart from each other by 2π/3; and d-q synchronous reference frame are built by direct axis (d-axis) and quadrature axis (q-axis), and rotary angle $\theta = \omega t$ is the angle between d-axis of the rotor and the axis of phase a phase reference axis, measured in the normal direction of the rotor [50], where ω is the system angular frequency.

The d-q transformation (also named park transformation) formula for the three-phase system space vectors (such as voltages, currents, and linkages) is as follows:

$$\begin{bmatrix} x_d \\ x_q \end{bmatrix} = \frac{2}{3}\begin{bmatrix} \cos\theta & \cos(\theta - 2\pi/3) & \cos(\theta + 2\pi/3) \\ -\sin\theta & -\sin(\theta - 2\pi/3) & -\sin(\theta + 2\pi/3) \end{bmatrix}\begin{bmatrix} x_a \\ x_b \\ x_c \end{bmatrix} \tag{3.11}$$

There is another way to obtain the d-q transformation. Firstly, the space vectors are transformed from a-b-c coordinates to α-β coordinates by Clarke transformation; then the transformation is done from α-β coordinates to d-q synchronous reference frame [43]. The following equations are obtained:

$$\begin{bmatrix} x^{(d)} \\ x^{(q)} \end{bmatrix} = \begin{bmatrix} \cos\theta & \sin\theta \\ -\sin\theta & \cos\theta \end{bmatrix} \cdot \begin{bmatrix} x^{(\alpha)} \\ x^{(\beta)} \end{bmatrix} \tag{3.12}$$

For single-phase systems, this transformation cannot be applied directly because there is only one variable available, while the d-q transformation needs at least two orthogonal variables [51]-[53]. The authors of reference [51] presented the extension of the d-q transformation for single-phase systems. The imaginary orthogonal vector of the original vector with the same amplitude is proposed and then an orthogonal plane made of the two variables is formed. Although the imaginary vector does not exist physically. The single-phase d-q transformation matches with the transformation to change from α-β to d-q reference frame. However, it is preferred to call the signals as real and imaginary instead of α and β. Because a different d-q harmonic mapping from that of the three-phase one is obtained by using this method.

Equation (3.9) in the *d-q* frame can be derived as:

$$\begin{aligned} v_d^{(dq)} = {} & a_{i3} \cdot \dddot{i}_g^{(dq)} + a_{i2} \cdot \ddot{i}_g^{(dq)} + \left(a_{i1} - 3a_{i3}\omega^2\right) \cdot \dot{i}_g^{(dq)} \\ & + \left(a_{i0} - a_{i2}\omega^2\right) i_g^{(dq)} + \underbrace{\left(a_{i3} \cdot \omega^2 - a_{i1}\right) \cdot \begin{bmatrix} 0 & \omega \\ -\omega & 0 \end{bmatrix}}_{K_i} \cdot i_g^{(qd)} \end{aligned} \tag{3.13}$$

where K_i represents the coupling network of the current loop. Then with the decoupling networks, i.e., $-K_i \cdot i_g^{(dq)}$, the transfer function of $i_g(s)/v_d(s)$ can be found from equation (3.13), i.e.,

$$\frac{i_g(s)}{v_d(s)} = \frac{1}{a_3 \cdot s^3 + a_2 \cdot s^2 + \left(a_1 - 3a_3\omega^2\right) \cdot s + \left(a_0 - a_2\omega^2\right)} \tag{3.14}$$

Similarly, the equation(3.10) in the d-q frame can be derived as:

$$\ddot{v}_{dc}^{(dq)} + a_{v2}\cdot\ddot{v}_{dc}^{(dq)} + \left(a_{v1} - 3a_{v3}\cdot\omega^2\right)\cdot\dot{v}_{dc}^{(dq)} + \left(a_{v0} - a_{v2}\cdot\omega^2\right)\cdot v_{dc}^{(dq)} + \underbrace{\left(\omega^2 - a_1\right)\begin{bmatrix}0 & \omega\\ -\omega & 0\end{bmatrix}}_{K_{v1}}\cdot v_{dc}^{(qd)}$$
$$+ b_2\ddot{v}_{com}^{(dq)} + b_1\dot{v}_{com}^{(dq)} + \left(b_0 - b_2\omega^2\right)v_{com}^{(dq)} + \underbrace{b_1\cdot\begin{bmatrix}0 & \omega\\ -\omega & 0\end{bmatrix}}_{K_{v2}}\cdot v_{com}^{(qd)} = 0 \qquad (3.15)$$

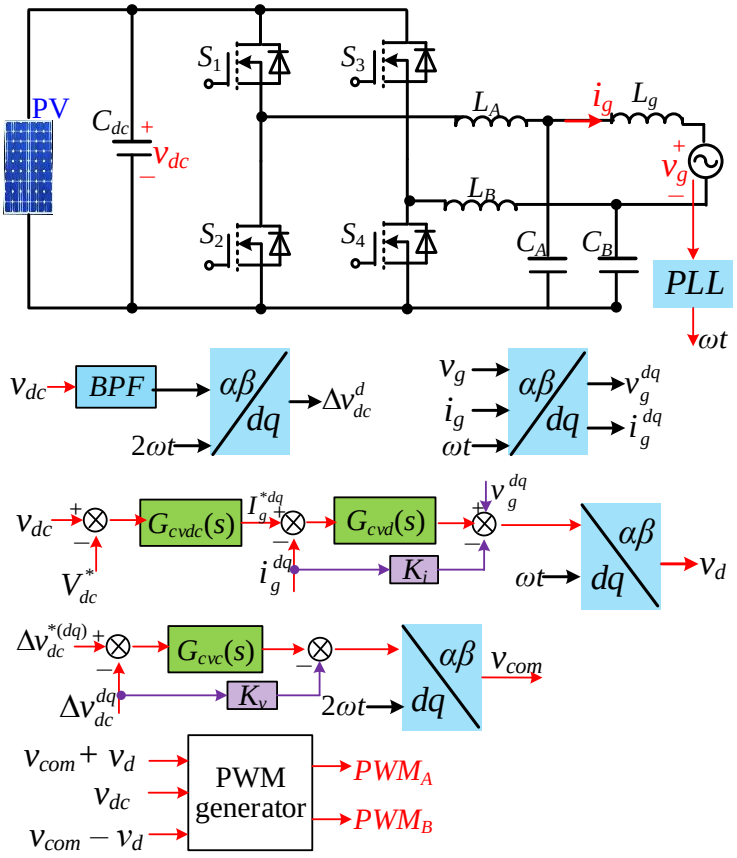

Figure 3.4 Signal flow of the overall system

where K_{v1} and K_{v2} represents the coupling network of the voltage loop. Then with the decoupling networks, i.e., $-K_{v1}\cdot v_{dc}^{(dq)}$ and $-K_{v2}\cdot v_{com}^{(dq)}$, the transfer function of $v_{dc}(s)/v_{com}(s)$ can be found from equation (3.15), i.e.,

$$\frac{v_{dc}(s)}{v_{com}(s)} = \frac{-b_{2v}s^2 - b_{1v}\cdot s - \left(b_{0v} - b_{2v}\cdot\omega^2\right)}{s^3 + a_{2v}\cdot s^2 + \left(a_{1v} - 3\omega^2\right)\cdot s + \left(a_{0v} - a_{2v}\cdot\omega^2\right)} \tag{3.16}$$

As indicated by equation (3.14) and equation (3.16), the transfer function in the d-q frame is a third order system and conventional PI controllers can be designed to control the output current and the DC-link voltage ripple. The overall signal flows is shown in Figure 3.4. As shown in Figure 3.4, BPF is the band pass filter, and there are three controllers, $G_{cvdc}(s)$, $G_{cvd}(s)$, and $G_{cvc}(s)$, which controls the DC link average voltage, grid current, and voltage ripple, respectively. Once the decoupling networks, e.g., $-K_i \cdot i_g^{(dq)}$ and $-K_{v1} \cdot \Delta v_{dc}^{(dq)}$, are applied, controllers of i_g and Δv_{dc} can be designed based on $i_g(s)/v_d(s)$ and $v_{dc}(s)/v_{com}(s)$, respectively.

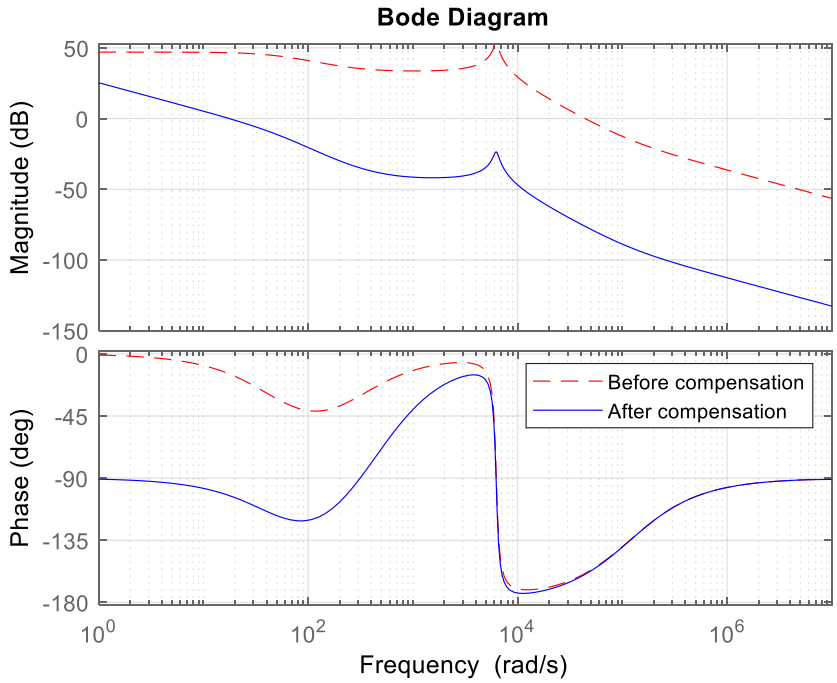

(a)

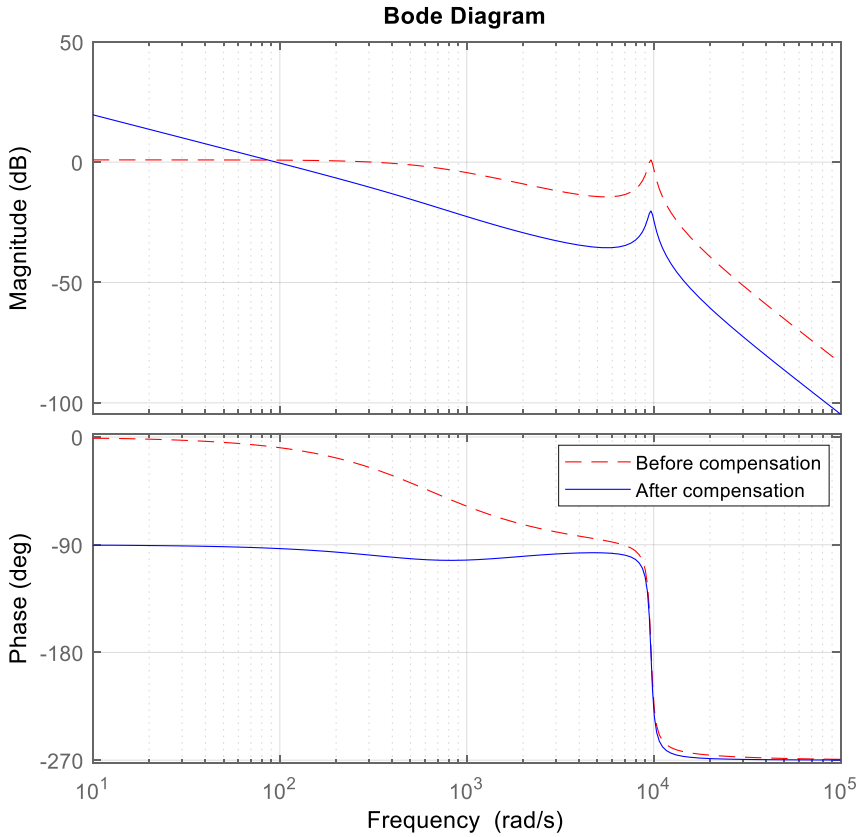

(b)

Figure 3.5 Bode plot of system before and after compensations. (a) $i_g(s)/v_d(s)$ with and without $G_{cvd}(s)$; (b) $v_{dc}(s)/v_{com}(s)$ with and without $G_{cvc}(s)$.

Figure 3.5 shows the bode plots of $i_g(s)/v_d(s)$ and $v_{dc}(s)/v_{com}(s)$ before and after using $G_{cvd}(s)$ and $G_{cvc}(s)$, respectively. As shown in Figure 3.5, the original current loop has high gain (≈ 50 dB) at its resonant peak, PI controller $G_{cvd}(s)$ which has the form of $k_p \cdot (s + k_i)/s$ is derived by suppressing gain at resonant frequency below – 20 dB. Similarly, $G_{cvc}(s)$ can be determined. Table I summarizes the controller parameters.

TABLE I: PARAMETERS OF CONTROLLERS

	$G_{cvd}(s)$	$G_{cvc}(s)$	$G_{cvdc}(s)$
k_p	8.64×10^{-2}	1.064×10^{-5}	1.54×10^{-4}
k_i	1000	1.2766×10^{6}	5.35×10^{2}

3.3 Experimental Results

A PV prototype is built to validate the proposed controllers. Figure 3.6 Experimental setup shows the experimental setup, where PV panel is emulated by a BK PVS60085MR programmable DC source; the control algorithm was implemented in eZdsp F28335. The open-circuit voltage and short-circuit current of PV panel are 220 V and 2.4 A, respectively, and the voltage corresponding to the maximum power (= 400 W) is around 180 V. $C_{dc} = C_A = C_B = 68$ μF, $L_2 = 470$ μH, $L_g = 940$ μH.

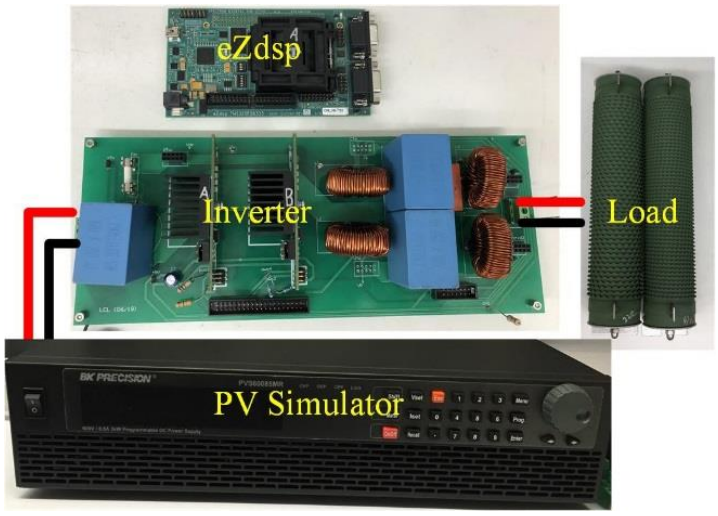

Figure 3.6 Experimental setup

Figure 3.7 shows the steady state waveforms of v_{dc}, i_g, d, and D. The peak-to-peak-value of the v_{dc} is 6.8 V, which indicates the power decoupling is mainly achieved

on the AC side. Due to the existence of D, the double frequency voltage ripple of the v_{dc} is eliminated.

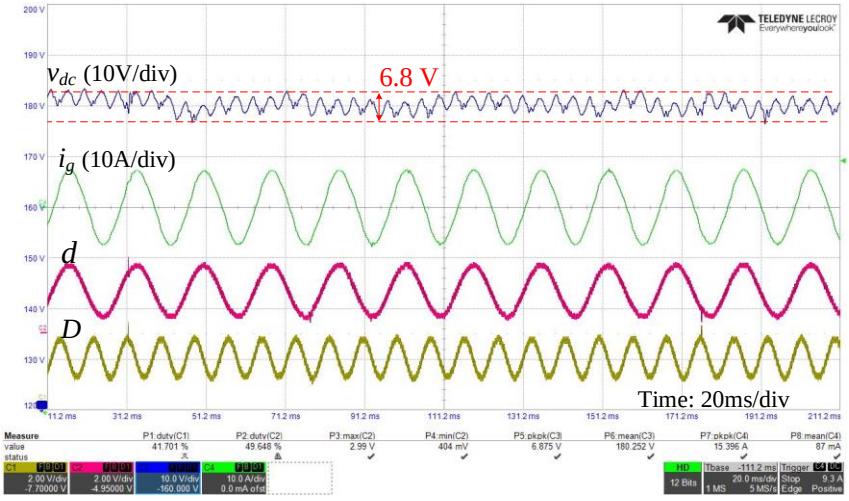

Figure 3.7 Steady-state waveforms of v_{dc}, i_g, d and D.

Figure 3.8 compares the steady state waveforms of v_{dc} and i_g without and with the use of $G_{cvc}(s)$. As shown in Figure 3.8(a), without $G_{cvc}(s)$, the dominant ripple component of v_{dc} is 120 Hz with the peak-to-peak value is approximate 25 V, the amount of decoupling power on the DC link is 115 W according to equation (3.1). Therefore, the rest 285 W power decoupling is achieved on the AC side, i.e., C_A and C_B. When $G_{cvc}(s)$ is used, the maximum peak-to-peak value of v_{dc} is 5 V, the calculated power decoupled on the DC side is around 11.5 W, which indicates 388 W power decoupling is achieved on the AC side. Therefore, the two-stage power decoupling can be controlled by regulating the DC-link voltage ripple, which validates the effectiveness of $G_{cvc}(s)$. The mean value can be controlled by regulating the DC-link voltage ripple, which validates the effectiveness of $G_{cvc}(s)$. The mean value of v_{dc} is close to 180 V and the output current i_g

is sinusoidal waveform and measured root mean square (RMS) value of i_g is 5.9 A, which testify $G_{cvdc}(s)$ and $G_{cvd}(s)$.

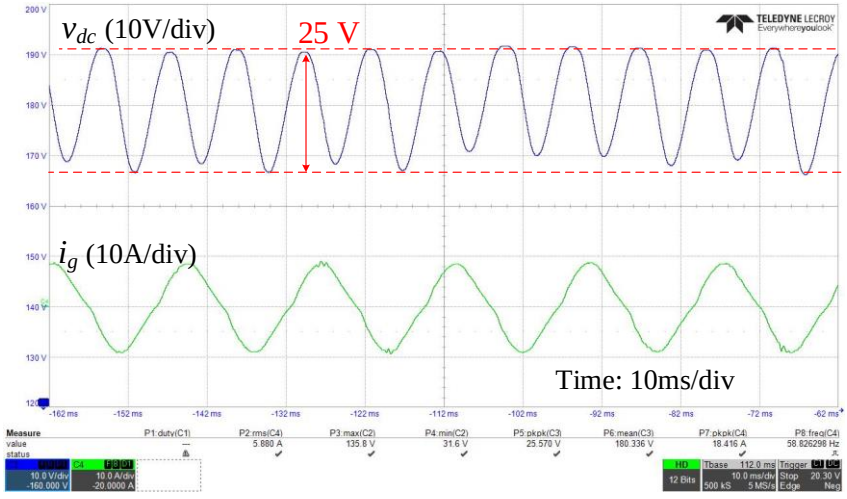

(a)

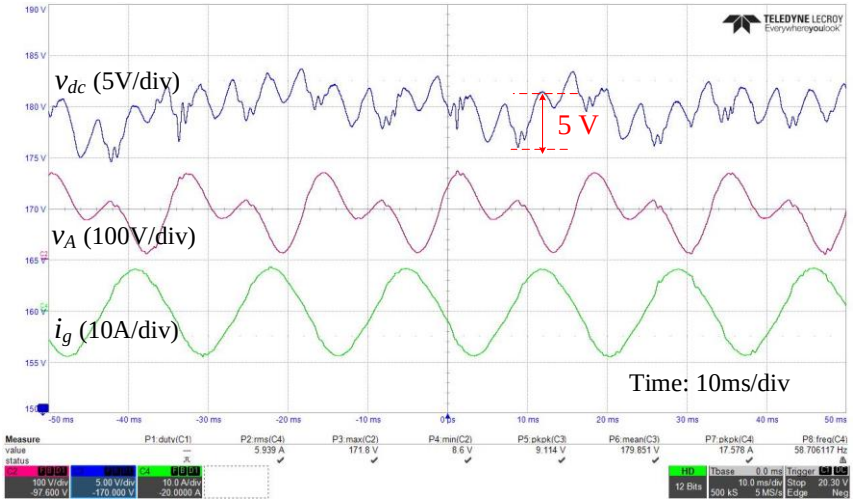

(b)

Figure 3.8 Comparison of steady-state waveforms. (a) Without $G_{cvc}(s)$; (b) with $G_{cvc}(s)$.

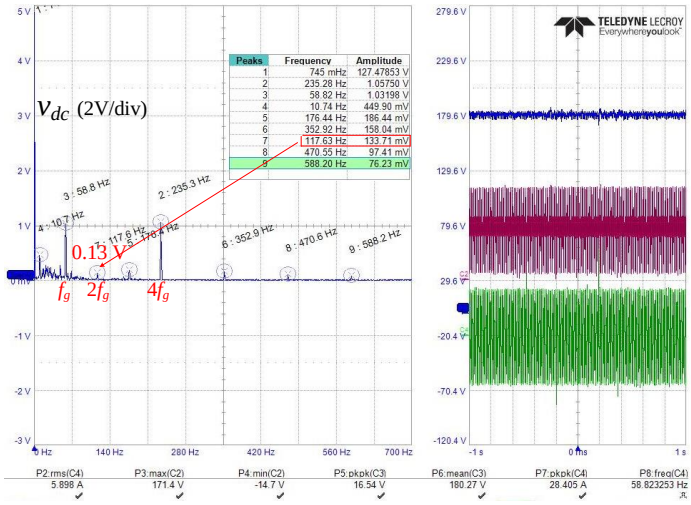

Figure 3.9 Spectrum of v_{dc} with $G_{cvc}(s)$.

Figure 3.9 compares the spectrum of v_{dc} when $G_{cvc}(s)$ is used, the traditional harmonic at $2 \cdot f_g$ is suppressed close to zero, the dominant ripple components are changed to the 1st and 4th order, their magnitudes, i.e., 1 V, are less than 10V. It should be noted that if the power is only decoupled on the DC link to control the ripple of 5 V, the capacitance value of C_{dc} is 900 μF thus the film capacitor which has high reliability cannot be used.

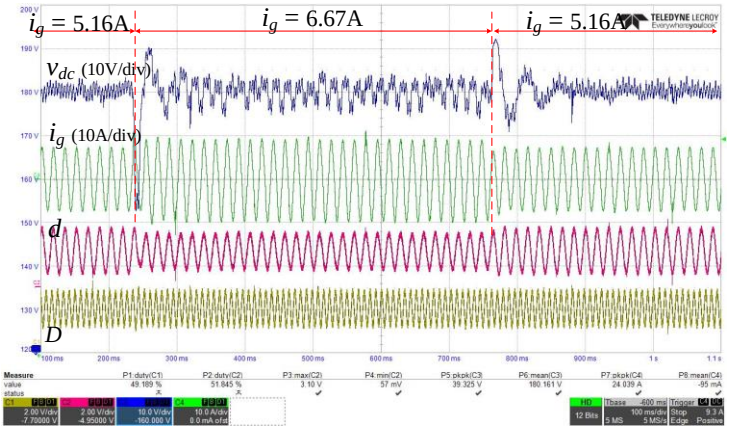

Figure 3.10 Transient response when the load changes.

Figure 3.10 shows the transient response when the load is changed. As shown in Figure 3.10, the frequency of v_d and v_{com} are 60 Hz and 120 Hz, respectively. At first, i_g = 5.16 A, the v_{dc} ripple is less than 3 V due to the existence of v_{com}. At t = 240 ms, i_g is changed to 6.67 A, the transient state lasts approximately 60 ms, during which v_{dc} first drops and then increases, the steady-state voltage ripple is around 5 V which is slightly higher than 3 V. At t = 760 ms, i_g is changed back to 5.16 A, v_{dc} has around 12-V overshoot then drops back to 180 V, which again validates the effectiveness of the three designed controllers.

3.4 Summary

This chapter presented modeling and control of a two-stage power decoupled PV inverter. The power decoupling can be achieved on both DC and AC sides, then the film capacitors with smaller capacitance can be used on DC-link. Besides, by modeling the inverter in the d-q frame, the conventional PI controllers can be designed to remove the pulsating power. The experimental results showed the capacitor at DC bus can be significantly reduced from 900 μF to 68 μF while maintaining the same voltage ripple. The use of film capacitors will further increase the life span and the reliability of the PV inverter.

Chapter 4 : A Composite Power Decoupling Method with Optimized Energy Buffer

As mentioned in chapter 2, there are two categories of the power decoupling according to the use of the active switch or not, the passive power decoupling (PPD) and active power decoupling (APD).

The traditional PPD solution places a capacitor on the PV side or DC-link [14]. The advantage of this solution is its simplicity and ease of implementation. However, because of the low frequency of the grid, either a large capacitor or a high voltage is required in this DC side passive power decoupling (DC-PPD). which requires larger energy buffer. Since the energy buffer is proportional to the capacitance and the voltage squared [8], large energy buffer is required. Hence the large capacitance or high voltage rating in DC-PPD requires bulky and less reliable electrolytic capacitor.

To reduce the capacitance (or energy buffer), numerous APD methods with additional circuits or power electronics devices are used [53]-[55]. These APD methods are implemented by either adding an extra bidirectional converter, e.g., buck-boost converter [53],[55] or using complicated control algorithms for power decoupling [54], which increase the voltage or current stress of the added circuit and requires more powerful DSP [56]. Recently, AC side active power decoupling (AC-APD) methods were introduced without adding extra power electronics devices in the literature, e.g., introducing two capacitors on the AC side [20],[40], dynamic power decoupling strategy

to limit the maximum power ripple [57]. Introducing one phase [58] and doubling ground with dynamic DC-link voltage [59]. However, the traditional PI controller cannot be used due to its low gain at the double grid frequency. The use of parameter dependent controller may not achieve satisfactory compensation in case there are parameter drifts in the system [60]-[61]. Moreover, it requires too many measurements, and they are focus on either DC or AC side power decoupling, capacitance is optimized on either side thus the total capacitor volume is not minimized.

In this paper, a composite power decoupling (CPD) is proposed to address the following issues: 1) optimization of the total capacitance includes both DC and AC sides while maintain high MPPT efficiency and low THDi; 2) supporting the double line frequency power with reliable film capacitor by using the developed CPD which can automatically activate or deactivate the DC-PPD; 3) modeling in d-q frame and develop PI controller with simple structure and fewer measurements [60].

The rest of the chapter is organized as follows. Section I illustrates power decoupling and energy buffer optimization. Section II discusses the modeling and controller design of the inverter. Detailed experimental results are provided in Section III. A brief conclusion is presented in Section V.

4.1 Power Decoupling and Energy Buffer Optimization

The overall configuration of the PV inverter is shown in Figure 3.1. Due to the added power decoupling capability, C_{dc} can be reduced so that the film capacitor which has longer lifetime and higher reliability than the electrolytic capacitor can be used. Unlike existing methods where the power decoupling is either realized on the DC or AC side, in this chapter, the power decoupling is achieved on both sides dynamically, therefore it has the merits of both passive and active power decoupling methods mentioned in Chapter 2.

The equation (2.1), as we mentioned before, shows that the instantaneous power of the inverter which works in the vicinity of unity power factor. P and $\tilde{p}$ represents average and pulsating power of the inverter, respectively. In this chapter, since power is decoupled on both DC and AC side, assuming $\varphi=0$, then the decoupling power can be expressed as:

$$S \cdot \cos(2\omega t) = p_{dc} + p_{ac} \tag{4.1}$$

Just do the average we can obtain:

$$P = P_{dc} + P_{ac} \tag{4.2}$$

where P_{dc} and P_{ac} are the power decoupled by DC-PPD and AC-APD, respectively.

4.1.1 DC Side Passive Power Decoupling

Like the traditional DC-PPD which is achieved by placing a capacitor on the DC link, the maximum amount of power decoupled on the DC bus can be calculated with the equation(3.1), where P_{dc} is the power decoupled by C_{dc}. Due to the size and

capacitance limitation of the film capacitor, the capacity of DC-PPD is limited. Considering the maximum allowance of Δv_{dc} should not be more than 5% of V_{dc} according to the IEEE standard 519, the maximum power decoupled on the DC side.

$$P_{dc,\max} = 0.1 \cdot \omega \cdot C_{dc} \cdot V_{dc}^2 \tag{4.3}$$

4.1.2 AC Side Active Power Decoupling

On the AC side, the pulsating power is removed by the two added capacitors, the decoupled power is

$$v_A \cdot \left(C_A \cdot \frac{dv_A}{dt} \right) + v_B \cdot \left(C_B \cdot \frac{dv_B}{dt} \right) = P_{ac} \cdot \cos(2\omega t) \tag{4.4}$$

Substituting $v_o = v_A - v_B$, $v_{A,B}$ (v_A and v_B) can be found:

$$v_{A,B} = \underbrace{\sqrt{\frac{P_{ac} \cdot \sin(2\omega t)}{2\omega \cdot C_2} + V_{c0}^2 - \frac{v_o^2}{4}}}_{v_{com}} \pm \underbrace{\frac{v_o}{2}}_{v_d} \tag{4.5}$$

where V_{c0} is the voltage of C_A and C_B when $t = 0$; $C_A = C_B = C_2$; $v_{com} = (v_A + v_B)/2$, and $v_d = (v_A - v_B)/2$. The duty cycles of the switch S_1 and S_3, $d_{A,B} = v_{A,B}/V_{dc}$.

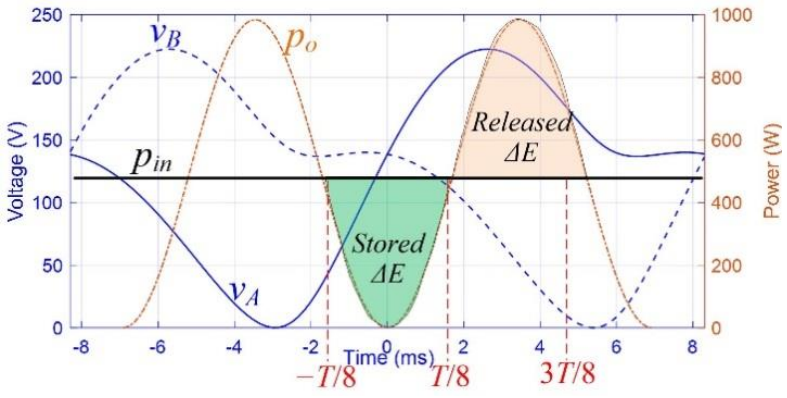

Figure 4.1 Ideal waveforms of v_A, v_B, p_{in}, and p_o.

Figure 4.1 shows the ideal waveforms of v_A, v_B, p_{in}, and p_o within one grid cycle, p_{in} is desired to be constant, two capacitors charge and discharge to remove the pulsated power of p_o, v_A and v_B are DC voltages and its difference v_o is sinusoidal waveform. According to equation (4.4), the value of P_{ac} is limited to maintain $0 \le v_{A,B} \le V_{dc}$. For a rated P_{ac}, it is necessary to find the minimum value of C_2. Then the relationship between the C_2 and P_{ac} should be found. As shown in Figure 4.1, during the range of $[-T/8, T/8]$, $p_{in} > p_o$, the pulsated energy absorbed by C_A and C_B can be found:

$$\Delta E = \frac{1}{2} \cdot C_2 \cdot \left[v_A^2\left(\frac{T}{8}\right) - v_A^2\left(\frac{-T}{8}\right) + v_B^2\left(\frac{T}{8}\right) - v_B^2\left(\frac{-T}{8}\right) \right] \tag{4.6}$$

Substitute v_A and v_B calculated from equation (4.5) into equation(4.6), then

$$\Delta E = C_2 \cdot V_{c0}^2 \tag{4.7}$$

During this period, as illustrated in Figure 4.1, the surplus energy stored in two capacitors is

$$\Delta E = \int_{-\frac{T}{8}}^{\frac{T}{8}} p(t) \cdot dt = \frac{P_{ac}}{\omega} \tag{4.8}$$

The decoupled power can be calculated as follows:

$$P_{ac} = \omega \cdot C_2 \cdot V_{c0}^2 \tag{4.9}$$

Equation (4.9) indicates that the decoupled power is determined by both C_2 and V_{c0} under the constraint of equation (4.7). Since $0 \le v_{A,B} \le V_{dc}$, the minimum value of C_2 is achieved when $min(v_{A,B}) = 0$ and $max(v_{A,B}) = V_{dc}$ at the same time. By setting $v_A(\omega t) = 0$

and $v_A'(\omega t) = 0$, the minimum value of V_{c0} can be found when $\tan(\omega t) = -2$, the details is in appendix.

$$V_{c0,\min} = \frac{2}{\sqrt{3}} V_o \tag{4.10}$$

For any $V_{c0} \geq V_{c0,\min}$, $min(v_{A,B}) \geq 0$ can be guaranteed. Similarly, by setting $v_B(\omega t) = V_{dc}$ and $v_B'(\omega t) = 0$:

$$V_{c0,\max} = \frac{\sqrt{6}}{4} \cdot V_{dc} \tag{4.11}$$

since $V_{c0,\max} \geq V_{c0,\min}$, then $V_{dc} \geq 4\sqrt{2} \cdot V_o/3$, when $V_{c0,\min} = V_{c0,\max}$, $min(v_{A,B}) = 0$ and $max(v_{A,B}) = V_{dc}$ can be achieved at the same time, the power decoupling capability is maximized by a given C_2 and its value is:

$$P_{ac,\max} = \frac{3}{8} \cdot \omega \cdot C_2 \cdot V_{dc}^2 \tag{4.12}$$

4.1.3 Composite Power Decoupling

The amount of power decoupling by DC-PPD and AC-APD needs to be allocated with the load power. According to equation(3.1), the DC-link voltage ripple can be used for controlling the amount of power decoupled by DC-PPD.

Figure 4.2 shows the CPD control strategy by controlling the voltage ripple Δv_{dc}, where $\Delta v^*_{dc,1}$ and $\Delta v^*_{dc,2}$ are references at the steady-state and the starting process, respectively. As shown in Figure 4.2 (a), in the steady state, when $p < P_{ac,max}$, power will be decoupled on the AC side, $\Delta v^*_{dc,1} = 0$; when $P_{ac,max} < p < P_{max}$, the reference ripple

voltage is linearly increased with p and its value is limited to the predefined maximum value, i.e., $\Delta v_{dc,\max}$, when $p \geq P_{max}$.

$$\Delta v_{dc,1}^{*} = \begin{cases} 0 & p \leq P_{ac,\max} \\ \dfrac{P - P_{ac,\max}}{\omega \cdot C_2 \cdot V_{dc}} & P_{ac,\max} < p < P_{\max} \\ \Delta v_{dc,\max} & p \geq P_{\max} \end{cases} \tag{4.13}$$

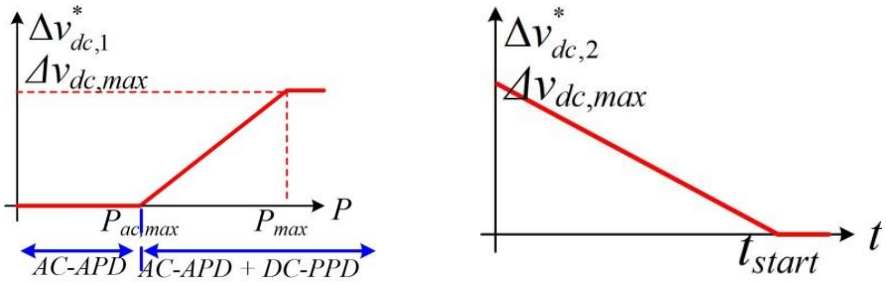

(a) (b)

Figure 4.2 Composite power decoupling control strategy. (a) Δv_{dc}^{*} in the steady state; (b) Δv_{dc}^{*} during the starting process.

During the starting processing, since it takes some time to measure the value of P, the power decoupling capacity is set as the maximum, i.e., $\Delta v_{dc}^{*} = \Delta v_{dc,\max}$, the reference voltage ripple will be linearly decreased to zero as shown in Figure 4.2 (b),then its values can be expressed:

$$\Delta v_{dc,2}^{*} = \Delta v_{dc,\max} - \frac{\Delta v_{dc,\max}}{t_{start}} \cdot t \qquad t \leq t_{start} \tag{4.14}$$

where t_{start} is the starting time of the inverter. Considering both (4.13) and (4.14) , the reference of the ripple voltage becomes:

$$\Delta v_{dc}^{*} = \max\left(\Delta v_{dc,1}^{*}, \Delta v_{dc,2}^{*}\right) \tag{4.15}$$

4.1.4 Capacitance Optimization

One function of inductors and capacitors is to control the current and voltage ripple at the switching frequency to meet the design requirement. Therefore, the minimum values need to be found before optimization.

$$\Delta I_A = \frac{V_{dc} - V_A}{L_2} \cdot d_A \cdot T = \frac{V_{dc} \cdot (1 - d_A) \cdot d_A}{f_s \cdot L_2} \tag{4.16}$$

where $L_A = L_B = L_2$; f_s is the switching frequency. Since $d_A \geq 0$, for a given $\Delta I\%$, the minimum L_2 is

$$L_{2,\min} = \frac{V_{dc} \cdot V_o}{8 f_s \cdot P \cdot \Delta I\%} \tag{4.17}$$

The change of electric charge at C_{dc} during the switching period $\Delta Q_{dc} = (\Delta I_A + \Delta I_B) \cdot T/2$ and the minimum value of C_{dc} is:

$$C_{dc,\min} = \frac{\Delta Q_{dc,\max}}{\Delta v_{dc,f_s}} = \underbrace{\frac{\Delta I\%}{f_s \cdot \Delta v_{dc,f_s}\%}}_{K} \cdot \frac{7 \cdot I_o}{8 \cdot V_{dc}} \tag{4.18}$$

where $\Delta v_{dc,fs}\% = \Delta v_{dc,fs}/V_{dc}$ is the voltage ripple at f_s. Similarly, the minimum value of C_2 can be found as follows:

$$C_{2,\min} = \frac{\Delta I_A \cdot d_A \cdot T}{2 \cdot \Delta v_{A,f_s}} = \frac{K \cdot I_o}{2 \cdot V_{dc}} \tag{4.19}$$

where K is defined in (4.18); $\Delta v_{A,fs}$ is the voltage ripple of v_A at f_s. Equation (4.18) and(4.19) indicate that for a given P and design criteria, the minimum capacitors are determined by f_s and V_{dc}. Then the objective function of the minimum energy stored in the capacitors can be expressed as follows:

$$\min \quad E = \frac{1}{2} \cdot C_{dc} \cdot V_{dc}^2 + C_2 \cdot V_{dc}^2$$

$$s.t. \begin{cases} 0.1 \cdot \omega \cdot C_{dc} \cdot V_{dc}^2 + 3/8 \cdot \omega \cdot C_2 \cdot V_{dc}^2 \geq P \\ \left(C_{dc} \cdot V_{dc}\right) \geq \left(C_{dc,\min} \cdot V_{dc}\right) = \dfrac{7K}{8} \cdot I_o \\ \left(C_2 \cdot V_{dc}\right) \geq \left(C_{2,\min} \cdot V_{dc}\right) = \dfrac{K}{2} \cdot I_o \end{cases} \tag{4.20}$$

Problem (21) is an optimization problem with power, minimum capacitance, and voltage constraints. Figure 4.3 shows the process of finding the optimization solution. The feasible solution area is determined by their constraints, i.e., $C_2 \geq C_{2,min}$, and $C_{dc} \geq C_{dc,min}$. Then power at point B is

$$P_B = \frac{11 \cdot \sqrt{2}}{30} \cdot \omega \cdot K \cdot P \approx 195.5 \cdot K \cdot P \tag{4.21}$$

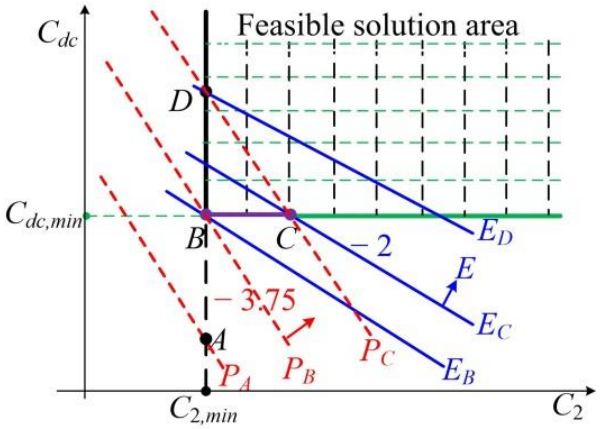

Figure 4.3 The feasible and optimal solutions.

Since the slope of E is – 2, which is larger than – 3.75 that corresponds to the power. Therefore, for the same power, $E_C < E_D$. The minimum energy buffer requirement can be found in the segment of BC.

$$\begin{cases} C_2^* \geq \dfrac{K \cdot I_o}{2 \cdot V_{dc}} \\ C_{dc}^* \leq \dfrac{7}{4} \cdot C_2^* \end{cases} \tag{4.22}$$

To make the optimum solution independent of the power rating, the value of K is properly designed to guarantee $P \leq P_B$, then the optimum solution is unique, i.e., point B ($C_{dc}^* = 1.75 \cdot C_2^*$) as illustrated in Figure 4.3.

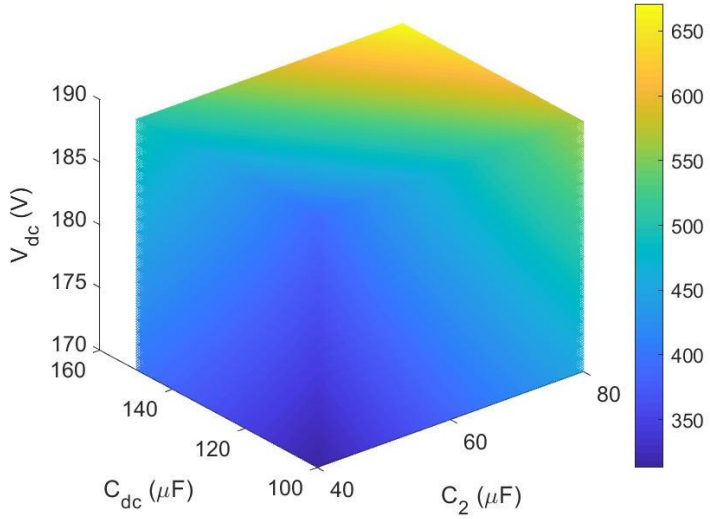

(a)

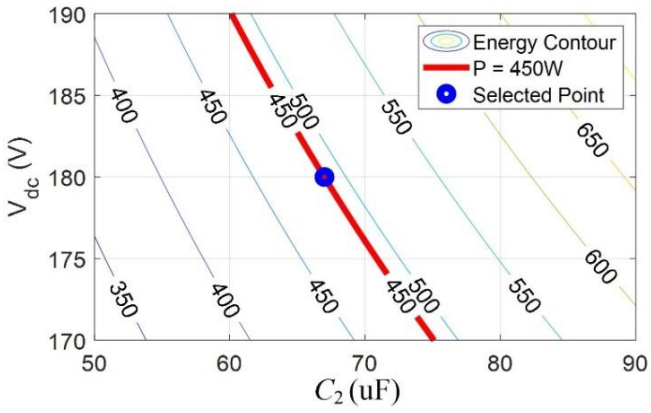

(b)

Figure 4.4 Power vs v_{dc}, C_{dc}, and C_2. (a) 4D view; (b) contour.

Figure 4.4 power vs V_{dc} and C_2 when the maximum $\Delta I\% = 25\%$ and $\Delta v\% = 0.3\%$. As shown in Figure 4.4, the decoupling power is increased with V_{dc} and C_2. The value of C_2 and V_{dc} can be selected from the curve, e.g., for P = 450 W, V_{dc} and C_2 can be selected to be 180 V and 67 μF, respectively. In this Chapter, C_2 = 68 μF, C_{dc} = 125 μF which is slightly higher than that calculated from equation (4.18).

Figure 4.5 compares the energy with different power decoupling methods. For a given P, use DC-PPD or AC-APD only requires more energy stored in capacitors than that with optimized CPD., e.g., when P = 450 W, the value of energy with DC-PPD, AC-APD and CPD are 1000 J, 620 J, and 480 J, respectively. Compared to DC-PPD and AC-APD, the capacitance (or energy buffer) can be reduced by 52% and 23% with the CPD.

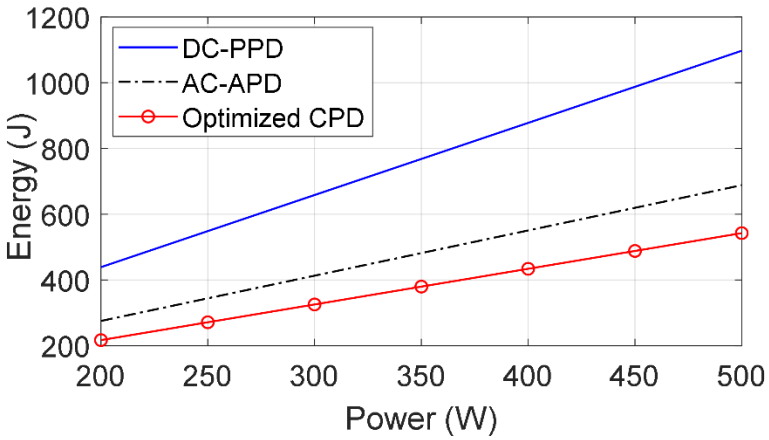

Figure 4.5 Comparison of energy with different power decoupling methods.

4.2 Modeling And Controllers Design in d-q Frame

Once the parameters of inverters are selected, the controllers of two-stage PV inverter are needed to be properly designed to achieve DC-PPD and AC-APD.

4.2.1 Modeling in the d-q Frame

With the average state-space method, the model of the PV inverter is expressed as equations from(3.3) to(3.10), and $i_o = i_g$, $v_c = v_{com}$. Define $d = (d_A - d_B)/2 = v_d/V_{dc}$. The transfer function $v_{dc}(s)/i_o(s)$ can be derived as

$$\frac{v_{dc}(s)}{i_o(s)} = -\frac{2 \cdot d}{C_{dc} \cdot s + 1/r_{pv}} \tag{4.23}$$

By applying the d-q transformation, equations of the differential and common mode signals in the *d-q* rotation frame can be found and listed in equations (3.13) and (3.15), which indicates that the output current (i_o) and voltage ripple (Δv_{dc}) can be controlled by differential and common mode voltages, respectively. K_i and K_v represents the coupling network of the current and voltage loop, respectively, with the decoupling networks, i.e., $-K_i \cdot i_o^{(dq)}$, $K_{v1} \cdot \Delta v_{dc}^{(dq)}$, and $-K_{v2} \cdot v_c^{(dq)}$, the transfer function of $i_o(s)/v_d(s)$ and $\Delta v_{dc}(s)/v_c(s)$ in the d-q frame can be found in equations (3.14) and (3.16).

4.2.2 Controllers Design

As indicated by equations (3.14) and (3.16), the transfer functions of $i_o(s)/v_d(s)$ and $\Delta v_{dc}(s)/v_c(s)$ in the d-q frame is a traditional third order system. In this paper, the PI controller with the form of $G_c(s) = k_p \cdot (s + k_i)/s$ is used.

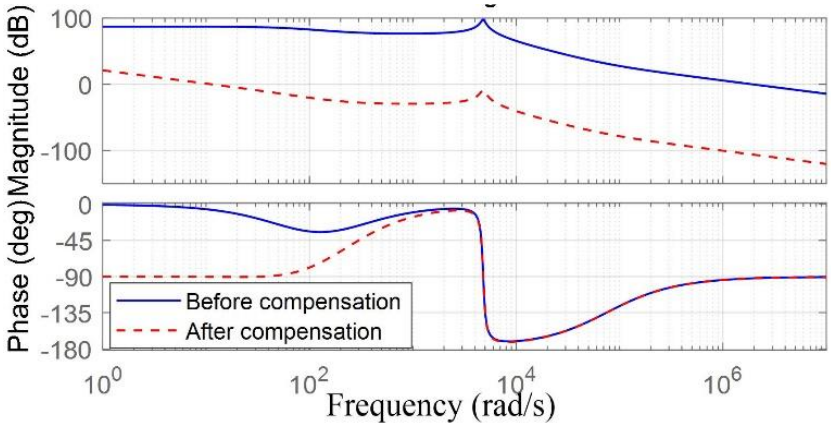

Figure 4.6 Bode plot of $\Delta v_{dc}(s)/v_c(s)$ before and after using $G_{cvc}(s)$.

Figure 4.6 shows the bode plots of $\Delta v_{dc}(s)/v_c(s)$ before and after using $G_{cvc}(s)$. As shown in Figure 4.6, the ripple voltage loop has high cutoff frequency and resonant peak around 1.6 kHz, $G_{cvc}(s)$ is derived by suppressing gain at resonant frequency below – 20 dB while maintaining its cutoff frequency lower than 120 Hz. Similarly, $G_{cvdc}(s)$ and $G_{cvd}(s)$ can be designed by setting their corresponding cutoff frequencies to be 30 Hz and 1 kHz, respectively. Table I summarizes three controllers' parameters.

TABLE I: Parameters of Controllers

	$G_{cvd}(s)$	$G_{cvc}(s)$	$G_{cvdc}(s)$
k_p	0.026	0.0025	0.5
k_i	72	100	90

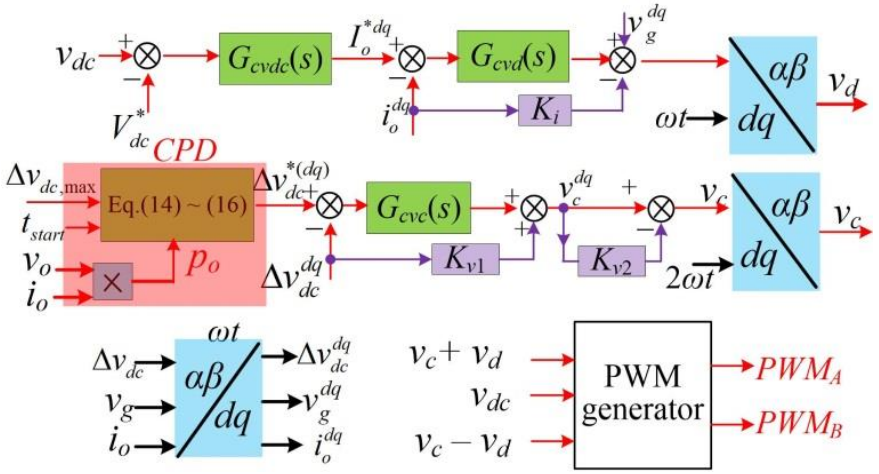

Figure 4.7 Signal flow of the overall system.

The overall signal flows are shown in Figure 4.7, where Δv_{dc} is extracted by a notch filter [26]. Three controllers, $G_{cvdc}(s)$, $G_{cvd}(s)$, and $G_{cvc}(s)$, controls the V_{dc}, i_o, and Δv_{dc}, respectively. The reference V_{dc}^* is determined by a MPPT controller to track the maximum power of the PV panel which is beyond the scope of this paper. $G_{cvc}(s)$ regulates Δv_{dc} which further controls the amount of power decoupled on the DC side. For example, when $\Delta v^*_{dc} = 0$, DC-PPD is inactive, power is decoupled by AC-APD. When $\Delta v^*_{dc} = 5\% \cdot V_{dc}$, both DC-PPD and AC-APD are active and maximum power decoupling capability is achieved.

4.3 Experimental Verification

A prototype of PV inverter is built to validate the proposed controllers. Figure 4.8 shows the experimental setup, where PV panel is emulated by a BK PVS60085MR programmable DC source; the maximum power is 420 W, the voltage corresponding to

the maximum power (V_{mpp}) is around 180 V. All film capacitors are used in the PV inverter, C_2 = 68 μF, C_{dc} = 125 μF, $L_2 = L_g/2$ = 470 μH, resistive load (R = 27 Ω) and nonlinear RCD load. Control algorithms are implemented in eZdsp F28335.

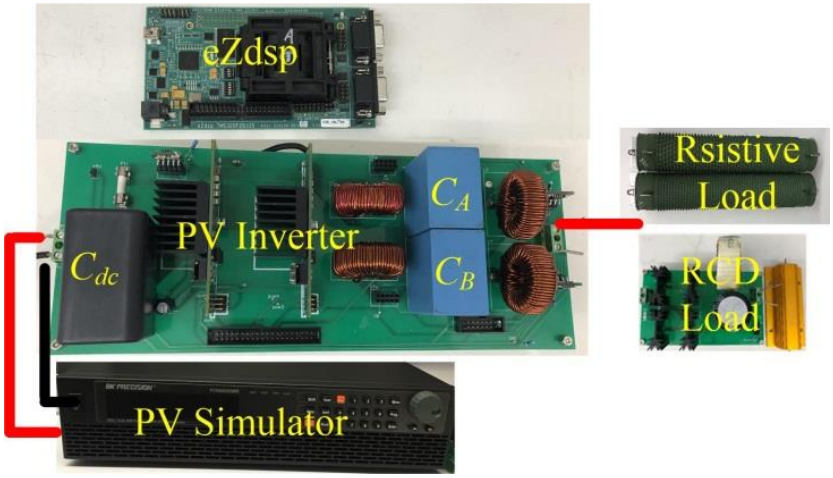

Figure 4.8 Experimental setup.

In the experiment, to avoid the parameters mismatch due to the tolerance of capacitance, voltage ripple, and efficiency of the inverter, P_{max} = 420 W and $P_{ac,max}$ = 310 W (≈ 74% P_{max}) which are slightly lower than the calculation.

4.3.1 AC-APD and its Optimization

To validate the optimization of capacitance, the input power first is set to be $P_{ac,max}$ so that the maximum power decoupling capability on the AC side can be observed, e.g., the maximum power of the PV panel is 308 W (< $P_{ac,max}$). Figure 4.9 shows the measured waveforms when the optimized parameters are used when the power is decoupled on the AC side, i.e., $V_{c0,\min} = V_{c0,\max}$, the mean value of v_{dc} is 181 V which is close to the V_{mpp} of the PV simulator, the measured peak-to-peak value of v_{dc} is 4.2 V,

then $\Delta v_{dc}\% = \Delta v_{dc}/(2V_{dc}) = 1.2$ %, such small Δv_{dc} indicates the power decoupling is mainly achieved AC-APD. Besides, as shown in Figure 4.9, the minimum and maximum values of v_B is 6 V and 176 V, respectively, these values are close to their ideal minimum and maximum values, i.e., values 0 V and 180 V, which indicates the maximum power decoupling capability is achieved with AC-APD.

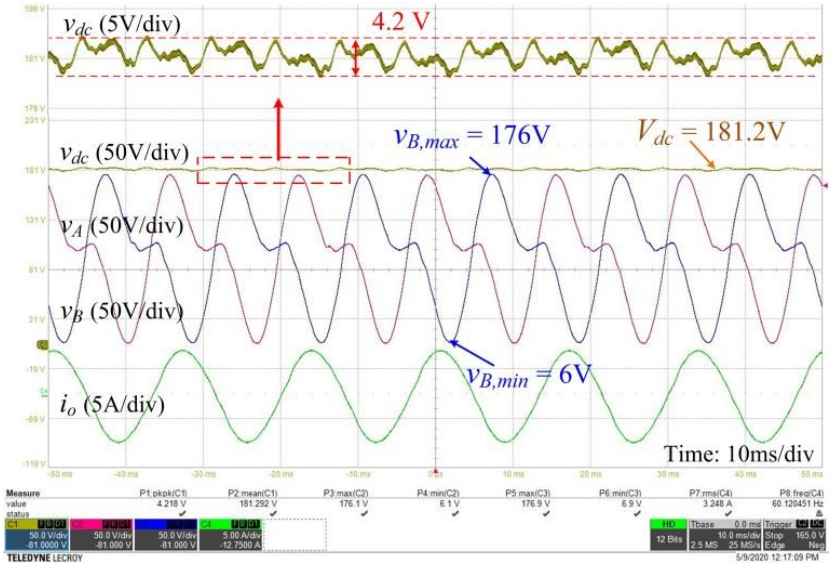

Figure 4.9 Measured waveforms when AC-APD is used.

Figure 4.10 shows the measured input and output power of the inverter, i.e., p_{in} and p_o. The average input power is constant with small oscillation, the value of 308 W indicates the inverter has achieved 99.3% MPPT efficiency. The measured output power is pulsated at 120 Hz, the minimum, mean, and maximum power are 0 W, 280W, and 579W, respectively. The measured average output power (P = 280 W) is lower than input 308 W because of the non 100% efficiency of the inverter.

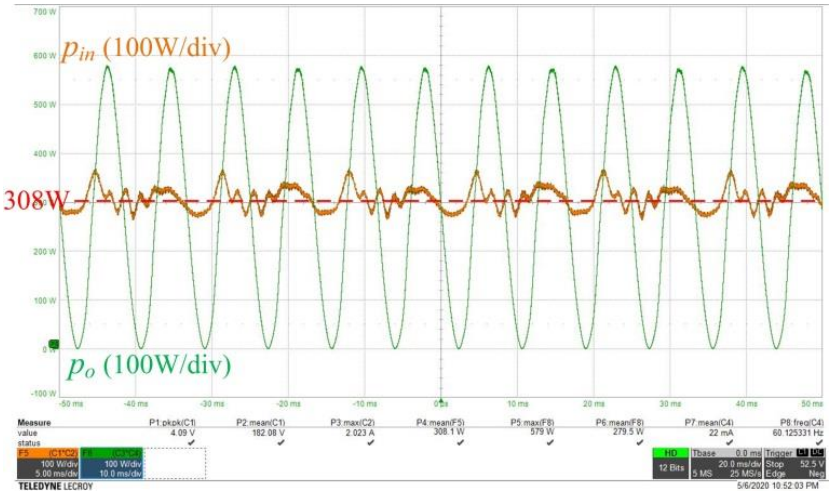

Figure 4.10 Measured input and output power of the inverter with AC-APD.

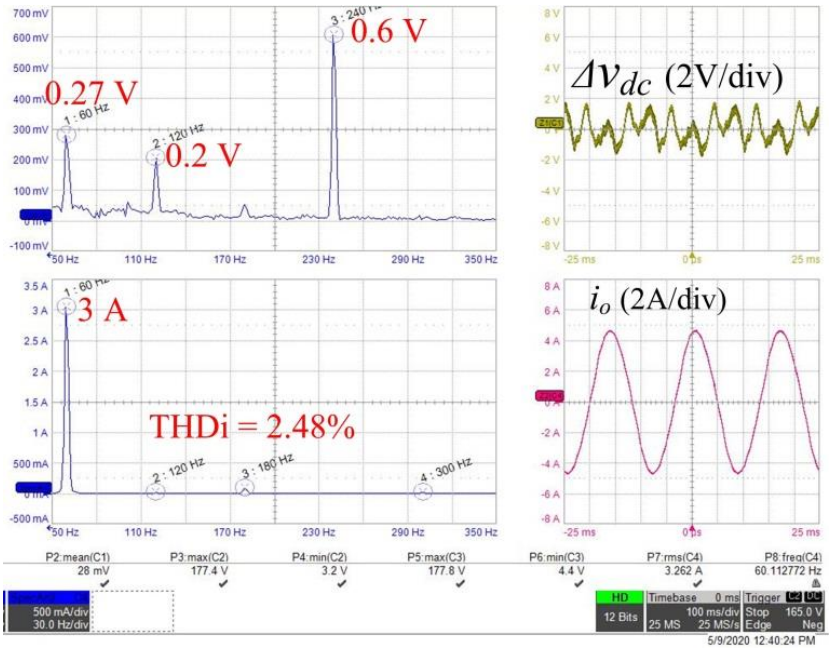

Figure 4.11 Spectrum of i_o with optimized AC-APD.

Figure 4.11 shows the spectrum of i_o with optimized AC-APD, the dominant ripple components of Δv_{dc} are 60 Hz and 240 Hz and their frequencies are 0.3 V and 0.6 V, the value of Δv_{dc} is less than 2 V, the THD of i_o is 2.48% due to the small Δv_{dc}.

4.3.2 Composite Power Decoupling

To validate the proposed CPD strategy, the solar power is step changed by abruptly connecting a 200 Ω resistor to the DC link. Then the DC side will be automatically deactivated when power is changed. In the experiment, $\Delta v_{dc,max}$ = 9 V so that the maximum power can be achieved while maintaining $\Delta v_{dc}\% < 5\%$, the starting time t_{start} = 1.2 sec.

Figure 4.12 shows measured waveforms when the input solar power is stepped changed from 420 W to 245 W. As shown in Figure 4.12 (a), the overall transient lasts approximately 60 ms, during which v_{dc} first drops and then increases, before and after the transient, V_{dc} is controlled to be 180 V, which further demonstrates the effectiveness of $G_{vdc}(s)$. The voltage ripple is decreased drastically after the transient, which indicates the DC-PPD is not active. During the whole transient, the magnitude of i_o changes but it has sinusoidal waveform.

When $t < -5$ ms as shown in Figure 4.12 (b), the input solar power (p_{in}) is 420 W, p_{in} oscillates and it has both 120 Hz and high frequency components, which indicates both DC-PPD and AC-APD are active. The peak-to-peak value of the Δv_{dc} is 16 V, which means the $P_{dc,max}$ is achieved and its value is around 135 W. The rest 285 W is decoupled on the AC side. Besides, as shown in Figure 4.12 (b), the minimum and maximum of v_A are 6.8 V and 176.4 V, which are close to that measured in Figure 4.9, therefore, the maximum power is decoupled on the AC side.

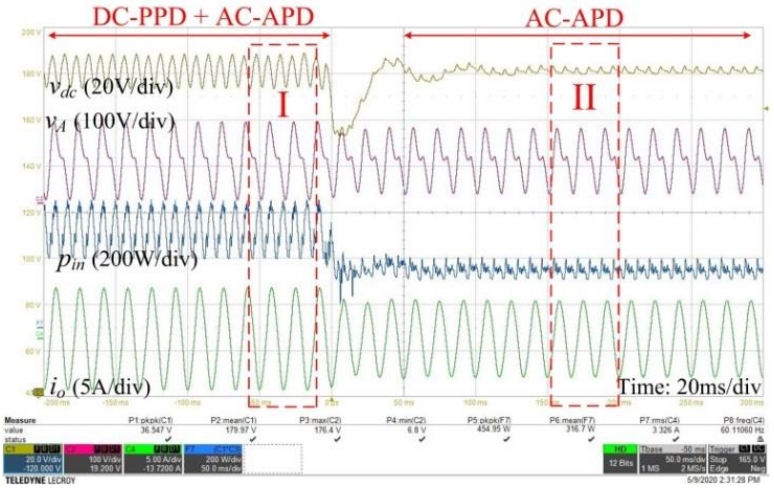
DC-PPD + AC-APD
AC-APD
v_{dc} (20V/div)
v_A (100V/div)
p_{in} (200W/div)
i_o (5A/div)
I
II
Time: 20ms/div

(a)

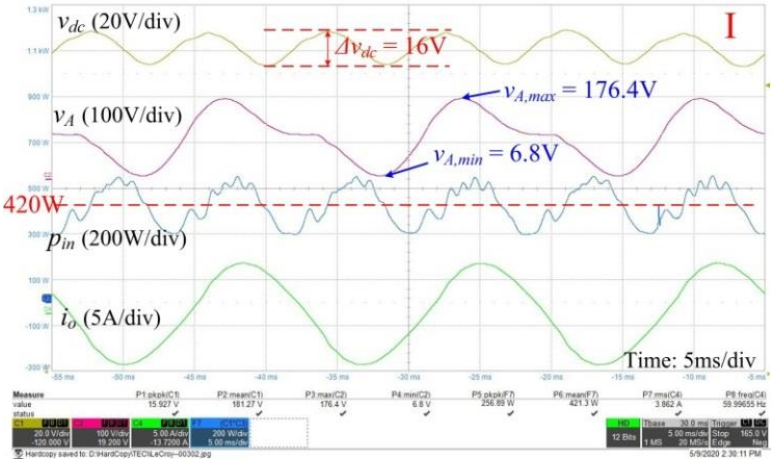
v_{dc} (20V/div)
Δv_{dc} = 16V
I
$v_{A,max}$ = 176.4V
v_A (100V/div)
$v_{A,min}$ = 6.8V
420W
p_{in} (200W/div)
i_o (5A/div)
Time: 5ms/div

(b)

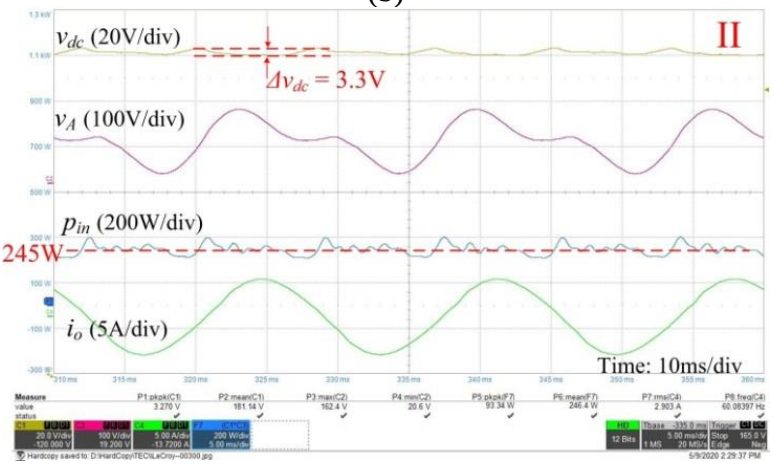
v_{dc} (20V/div)
Δv_{dc} = 3.3V
II
v_A (100V/div)
p_{in} (200W/div)
245W
i_o (5A/div)
Time: 10ms/div

(c)

Figure 4.12 Measured waveforms when p_{in} is step changed from 420 W to 245 W. (a) overall transient; (b) p_{in} = 420 W, both DC-PPD and AC-APD are active. (c) p_{in} = 245 W, only AC-APD is active.

When t > 300 ms as shown in Figure 4.12 (c), the measured p_{in} = 245 W (< $P_{ac,max}$), according to equation(4.13) , Δv^*_{dc} = 0 and the power is only decoupled on the AC side, which is validated from the measured low voltage ripple value, i.e., Δv_{dc} = 3.3 V.

Figure 4.13 shows the spectrum of i_o when p_{in} = 420 W. It should be noted that it is the worst case since the 16 V peak-to-peak value is close to its predefined maximum 18 V. The major component of the harmonic current is 0.15 A at 180 Hz, the calculated THDi is 4.34% which is less than 5%.

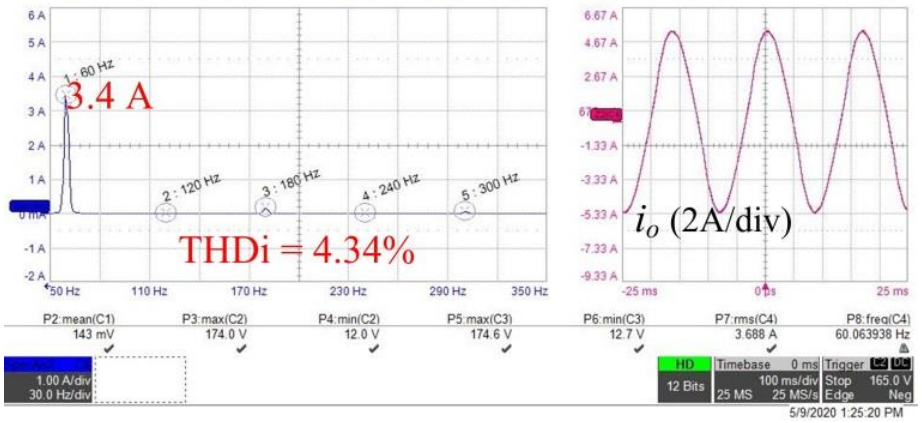

Figure 4.13 Spectrum of i_o when p_{in} = 420 W.

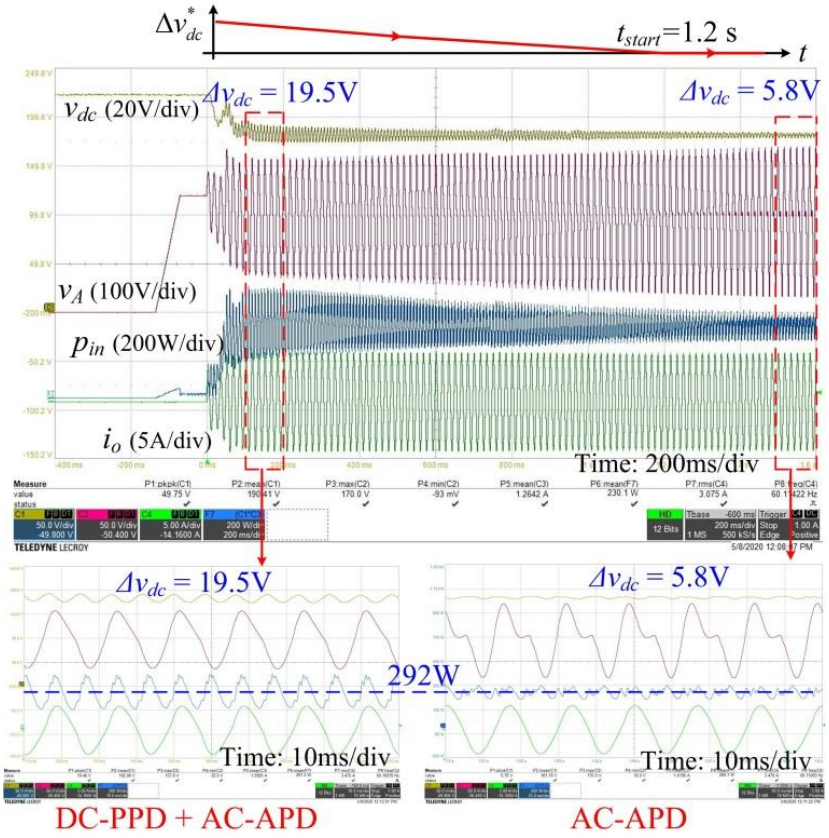

Figure 4.14 Measured waveforms during the starting process.

Figure 4.14 shows the measured waveforms during the starting process when P = 292 W. As shown in Figure 4.14, the measured Δv_{dc} decreases with the time, when t = 100 ms ($< t_{start}$), the peak-to-peak value of Δv_{dc} is 19.5 V, it is slightly higher than $2 \cdot \Delta v_{dc,max}$ (= 18 V), DC-PPD is active; when $t = t_{start}$, $\Delta v^*_{dc} = 0$ thus DC-PPD is not active; when t = 1.5 s ($> t_{start}$), the measured peak-to-peak value of Δv_{dc} is decreased to 5.8 V, it is close to that measured in Figure 4.9, which indicates the power is decoupled by AC-APD after t = 1.5 s.

4.3.3 MPPT Efficiency

As shown in Figure 4.9, when $p = P_{ac,max}$, the voltage ripple can be controlled less than 4.2 V, for such low ripple value, the high MPPT efficiency of the PV inverter can be guaranteed. When $p > P_{ac,max}$, DC-PPD is active, the MPPT efficiency decreases with the power. When $p = P_{max}$, MPPT efficiency is the lowest.

Figure 4.15 shows the measured waveform of v_{dc}, i_{pv} and the PV curve when the maximum power point (MPP) is set to be 420 W. The measured mean value of v_{dc} is 180 V, the peak-to-peak value of v_{dc} is 17.8 V. Figure 4.15 (b) shows the PV curve in the vicinity of MPP within Δv_{dc} is 17.8 V. When v_{dc} changes between 171 V and 189 V, the PV current decreases from 2.4 A to 2.2 A, the power corresponding to the minimum and maximum v_{dc} are 412.8 W and 413.6 W, respectively. The measured average input power is 415.8, which indicates the 98.9% MPPT efficiency is achieved. Therefore, when $p < P_{max}$, more than 99% MPPT efficiency can be guaranteed due to the low voltage ripple is achieved.

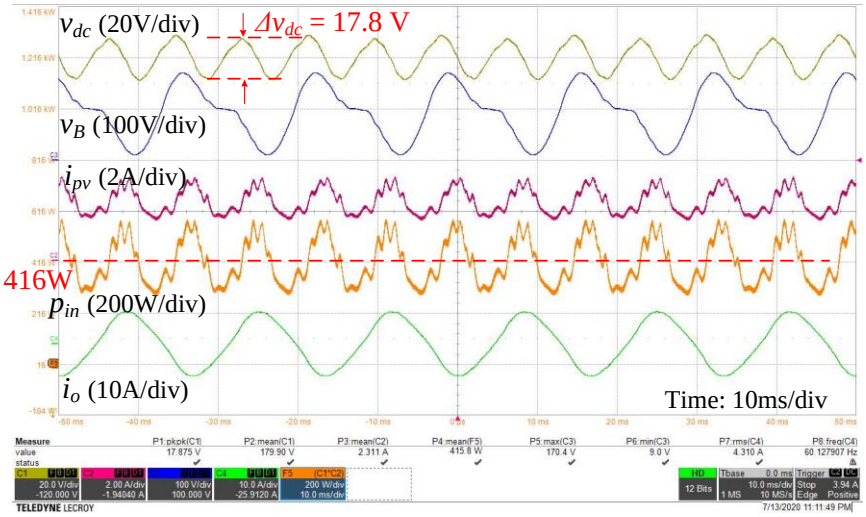

(a)

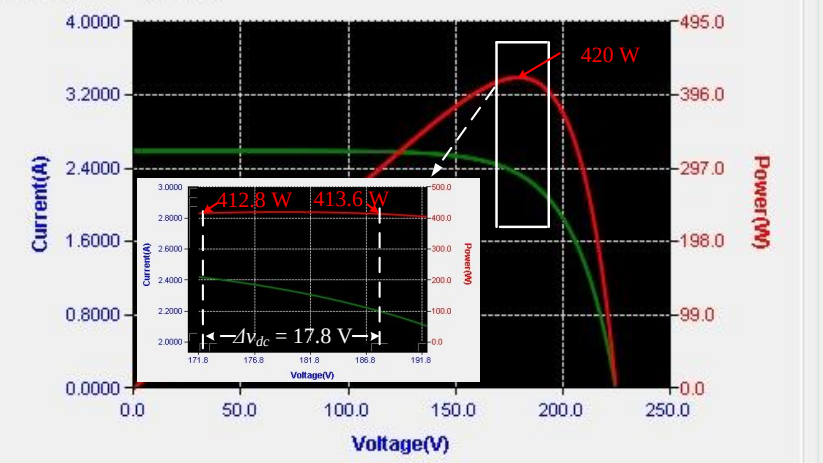

(b)

Figure 4.15 MPPT result when $p = P_{max}$. (a) Measured waveforms of v_{dc}, i_{pv}, and p_{in}; (b) PV curve when MPP is 420 W.

4.3.4 Performance Comparisons

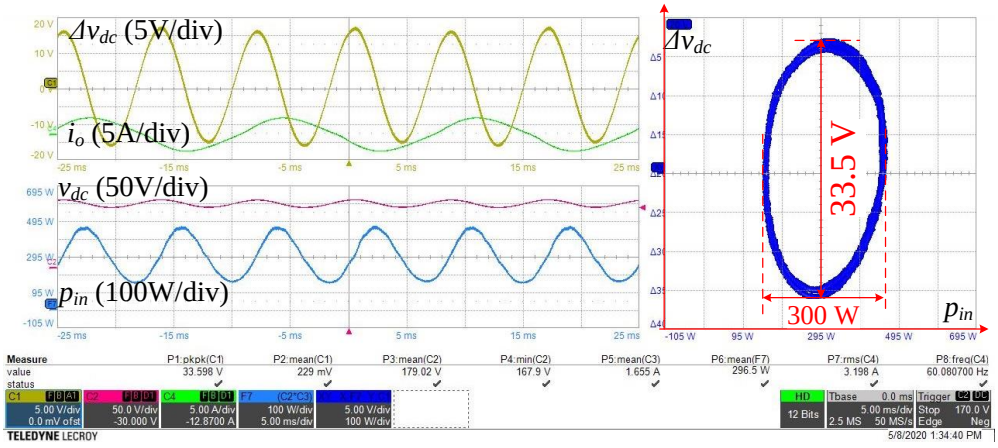

Figure 4.16 Measured waveforms when power is decoupled by DC-PPD.

To demonstrate the superiority of CPD when $p < P_{ac,max}$, the DC-PPD is compared. Figure 4.16 shows the measured waveforms when $G_{cvc}(s)$ is deactivated, i.e., only DC-PPD is active, the dominant ripple component of v_{dc} is 120 Hz and its peak-to-peak values is 33.5 V, $\Delta v_{dc}\%$ = 9.3 % (> 5%), therefore, a large C_{dc} is required to reduce the ripple voltage. Furthermore, due to the larger DC-Link voltage ripple, the input power pulsates at 120 Hz with magnitude is 150 W. The measured input power is 295 W and MPPT efficiency is 95%, which indicates less power is derived compared to CPD.

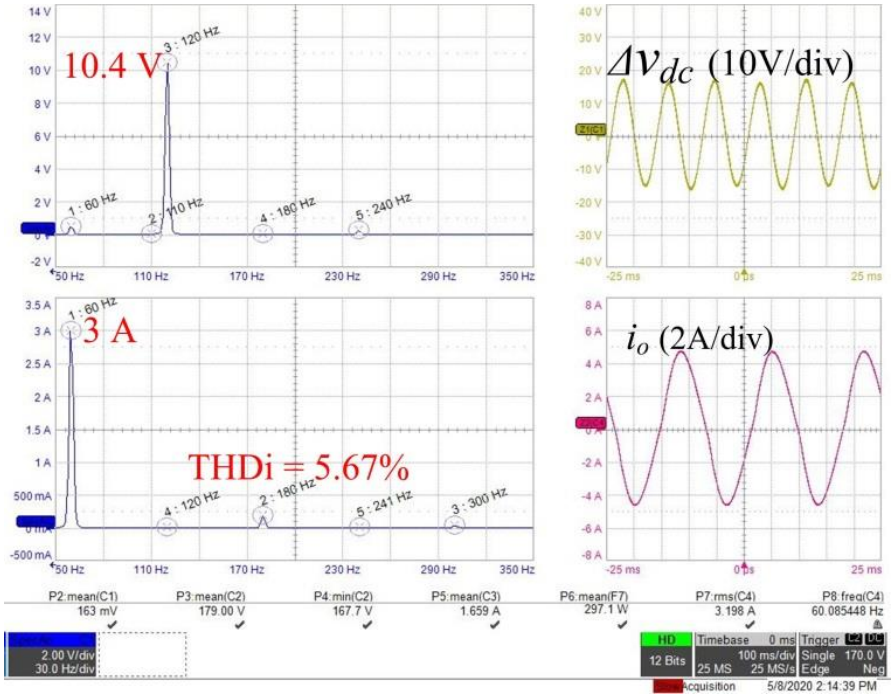

Figure 4.17 Spectrum of Δv_{dc} and i_o when power is decoupled by DC-PPD.

Figure 4.17 further compares their spectrum. As shown in Figure 4.17, when power is decoupled by DC-PPD, Δv_{dc} has dominant component at 120 Hz and its rms value is 10.4 V, the calculated THD of i_o is 5.67%; when AC-APD is used, the 120 Hz

ripple is suppressed to 0.2 V as shown in Figure 4.11. It should be noted that if the DC-PPD is used to achieve the ripple of 2 V, the required C_{dc} is 1300 μF, thus electrolytic capacitors are used. Therefore, when $p < P_{ac,max}$, AC-APD is preferred due its low DC-Link voltage ripple, lower THDi, and higher MPPT efficiency than DC-PPD.

To compare the DC-link voltage ripple and the MPPT efficiency, the traditional DC-PPD with large capacitors are compared. Table II compared the capacitance when Δv_{dc} is 4.2 V (at $P_{ac,max}$) and 18 V (at P_{max}) with different power decoupling methods.

TABLE II: TOTAL CAPACITANCE OF THREE METHODS

	Δv_{dc} = 4.2 V @ $P_{ac,max}$		Δv_{dc} = 18 V @ P_{max}	
	C_{dc}	C_2	C_{dc}	C_2
CPD (261 μF)	125 μF	2·68 μF	125 μF	2·68 μF
DC-PPD (1120 μF)	1100 μF	20 μF		
DC-PPD (363 μF)			343 μF	20 μF

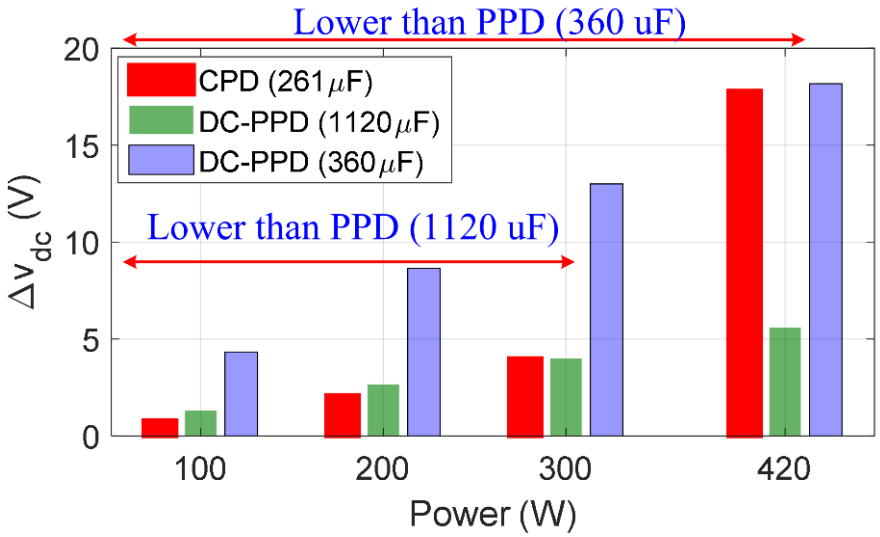

Figure 4.18 Comparison of Δv_{dc} with different decoupling methods.

As shown in the Table II, the calculated capacitance are 1120 μF and 363 μF to achieve the same Δv_{dc} at $P_{ac,max}$ and P_{max}, respectively. In the experiment, 343 μF is used in C_{dc}. Figure 4.18 compares the Δv_{dc} with different methods. When $p < P_{ac,max}$ (310 W), CPD has the lowest Δv_{dc}, i.e., CPD with 261 μF has higher MPPT efficiency than DC-PPD with 1120 μF. When $p = P_{max}$, CPD has similar Δv_{dc} with DC-PPD (360 μF), however, when $p < P_{max}$, CPD has lower Δv_{dc} than DC-PPD (360 μF).

4.3.5 Nonlinear Load

To further test the effectiveness of the proposed method, the PV inverter is connected to a nonlinear load. In this thesis, a RCD type load which consists of a full-bridge rectifier built with diodes, a capacitor, and a resistor is used. Figure 4.19 shows the steady-state waveforms of v_{dc}, v_A, v_o and i_o with the nonlinear RCD load.

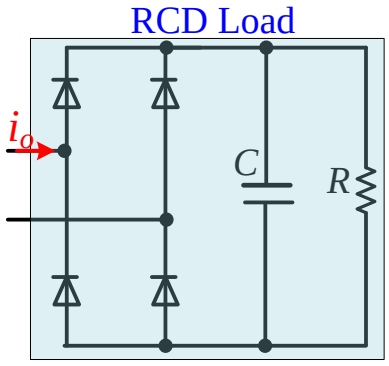

(a)

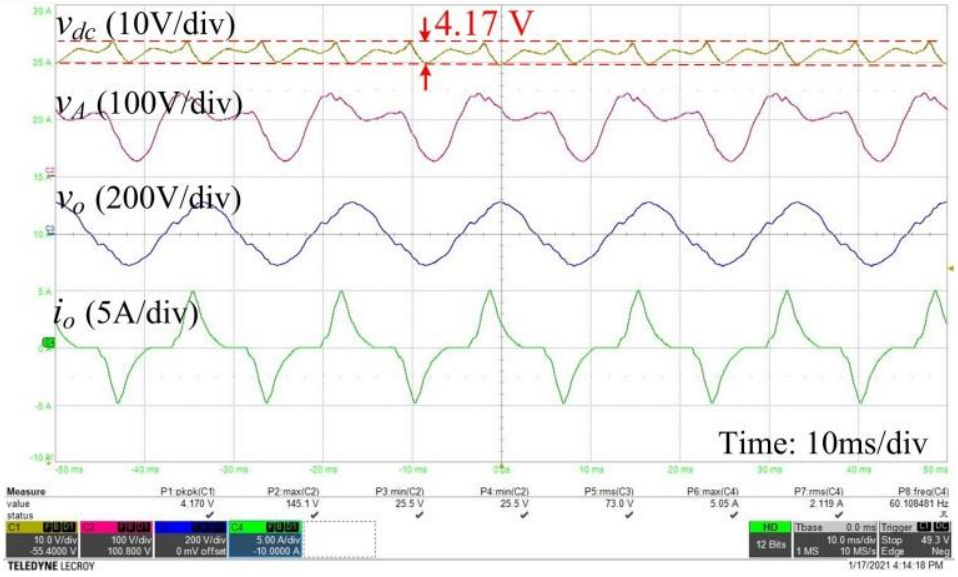

(b)

Figure 4.19 Measured steady-state waveforms with the RCD load. (a) Diagram of RCD load; (b) experimental result

As shown in Figure 4.19, i_o has high nonlinear characteristics, i.e., when v_o is less than a threshold voltage, $i_o = 0$, the power is only delivered through the rectifier when v_o is higher than the threshold voltage. The measured power is around 150 W, measured ripple voltage of the v_{dc} is 4.17 V, it is much less than the calculated 17.6 V, which validated the high MPPT efficiency can be achieved under the nonlinear load.

4.4 Summary

This chapter presents a composite DC-PPD and AC-APD for a PV inverter without adding extra power electronics devices. The novelty of the proposed method is that it minimizes the energy buffer and uses simple controller with less measurements

than the existing methods. First, the capacitance on both DC and AC side is optimized so that the more reliable film capacitors can be used. Then the inverter model derived in the d-q frame simplifies controllers' structure so that traditional PI controllers can be used. The proposed power decoupling method is validated on a 420 W prototype PV inverter. The experimental results show that the decoupling power can be automatically allocated according to the load power under the different conditions, e.g., both steady-state and the transient. Meanwhile, the maximum 99% MPPT efficiency and low THD are achieved in both linear resistive and nonlinear RCD loads.

Chapter 5 : Conclusions and Recommendations for Future Work

5.1 Conclusions and Contributions

The objective of this thesis research is to develop and implement power decoupling method for a single-phase PV inverter. The research work mainly includes: the power decoupling implementation in the d-q rotation frame, and power decoupling circuit optimization and propose a composite power decoupling method. The details conclusions and contributions are listed as follows:

1) **Power decoupling control in d-q frame**: The power decoupling control algorithm designed in the traditional static frame usually has relative complex structure, e.g., proportional resonant (PR) controller, the implementation is relatively difficulty. In this work, by modeling the circuit in the d-q rotation frame, the model as well as the controller is simplified, then the conventional PI controller can be easily derived and implemented in current DSP.
2) **An optimized composite power decoupling method**: The proposed composite power decoupling method consists of both passive and active power decoupling on DC and AC sides, respectively. On one hand, the energy buffer, e.g., capacitor for power decoupling, is minimized; on the other hand, the amount of power decoupled on DC and AC side is automatically changed to minimize the PV voltage ripple so that the maximum MPPT efficiency is achieved.

5.2 Recommendations for Future Work

Recommendations for further research are listed as follows:

Power decoupling in two-stage PV inverter: the proposed power decoupling method is for a single stage PV conversion, for most of applications, two-stage PV inverter is used, the power decoupling can be achieved by low and high DC sides and AC sides, then the allocation strategy of amount of power decoupled on three sides needs to be further developed to optimize the power decoupling. To achieve this, the DC-link voltage ripple can be increased to decrease the capacitance. Particularly, the dynamically changed voltage ripple on the DC link can mitigate the voltage ripple on the PV side, the MPPT efficiency can be guaranteed.

Power decoupling for grid-connected PV inverter: the proposed method is used in the standalone PV system, it regulates the output voltage of the inverter. While most of applications are for the grid-connected system, i.e., regulating sinusoidal current, then many other issues such as the synchronization and common mode current needs to be solved.

Bibliography

[1] Chakraborty, Arindam, "Advancements in power electronics and drives in interface with growing renewable energy resources," *Renewable & Sustainable Energy Reviews, Elsevier*, vol. 15, no. 4, pp.1816-1827, May, 2011.

[2] Renewable Energy Today and Tomorrow, Proceedings of the IEEE, vol. 89, no. 8, Aug. 2001.

[3] C. Hua, Y. Fang, C. Wong, “Improved solar system with maximum power point tracking,” *IET Renew. Power Gener.* Vol. 12, no. 7, pp. 806-814, May 2018.

[4] https://www.energy.gov/eere/bioenergy/biomass-resources

[5] REN21, "Renewables 2013: Global Status Report (GSR)," [Online]. Available: http://www.ren21.net/, Jun. 2013.

[6] REN21, "Renewables 2019: Global Status Report (GSR)," [Online]. Available: https://www.ren21.net/wpcontent/uploads/2019/05/gsr_2019_full_report_en.pdf.

[7] https://cleanenergynews.ihsmarkit.com/research-analysis/global-renewable-capacity-growth-at-record-in-2021-and-will-ac.html

[8] REN21, "enewables 2020: Global Status Report (GSR)," [Online]. Available: https://www.ren21.net/reports/global-status-report/ Jun. 2020

[9] https://www.iea.org/reports/renewables-2021?utm_source=SendGrid&utm_medium=Email&utm_campaign=IEA+newsletters

[10] E. Kabir, P. Kumar, S. Kumar, A. Adelodun, k. Kim, “Solar energy: Potential and future prospects,” *Renewable and Sustainable Energy Reviews*, vol. 82, no.1, pp. 894-900, Feb. 2018.

[11] Y. Zheng, D. Hill, Z. Dong, "Multi-agent optimal allocation of energy storage systems in distribution systems", *IEEE Trans. Sustainable Energy*, vol. 8, no. 4, pp. 1715-1725, 2017.

[12] A. R. Sparacino, G. F. Reed, R. J. Kerestes, B. M. Grainger and Z. T. Smith, "Survey of battery energy storage systems and modeling techniques," *2012 IEEE Power and Energy Society General Meeting*, 2012, pp. 1-8.

[13] https://en.wikipedia.org/wiki/Solar_energy

[14] H. Hu, S. Harb, N. Kutkut, and Z. Shen, “A review of power decoupling techniques for with three different decoupling capacitor locations in PV systems” *IEEE Trans. Power Electron.*, vol. 28, no. 6, pp. 2711-2726, June. 2013.

[15] Y. Sun, Y. Liu, M. Su, W. Xiong, and J. Yang, "Review of active power decoupling topologies in single-phase systems," *IEEE Trans. Power Electron.*, vol. 31, no. 7, pp. 4778-4794, July. 2016.

[16] S. Harb, H. Hu, N. Kutkut, I. Batarseh, and Z. Shen, “A three-port photovoltaic (PV) micro-inverter with power decoupling capability,” in *Proc. IEEE Appl. Power Electron. Conf. Expo.*, Fort Worth, TX, Mar. 2011, pp. 203-208.

[17] T. Shimizu, K. Wada, and N. Nakamura, “Flyback-type single-phase utility interactive inverter with power pulsation decoupling on the DC input for an AC photovoltaic module system,” *IEEE Trans. Power Electron.*, vol. 21, no. 5, pp. 1264-1272, Sept. 2006.

[18] C. Liao, W. Lin, Y. Chen, and C. Chou, “A PV micro-inverter with PV current decoupling strategy,” *IEEE Trans. Power Electron.,* vol. 32, no. 8, pp. 6544-6557, Aug. 2017.

[19] M. Vitorino, L. Alves, R. Wang, and M. Rossiter Corrêa, "Low-frequency power decoupling in single-phase applications: A comprehensive overview," *IEEE Trans. Power Electron.,* vol. 32, no. 4, pp. 2892-2912, April. 2017.

[20] I. Serban, “Power decoupling method for single-phase h-bridge inverters with no additional power electronics,” *IEEE Trans. Ind. Electron.*, vol. 62, no. 8, pp. 4805-4813, Aug. 2015.

[21] E. Makovenko, O. Husev, J. Zakis, C. Roncero-Clemente, E. Romero-Cadaval, and D. Vinnikov, "Passive power decoupling approach for three-level single-phase impedance source inverter based on resonant and PID controllers," *2017 11th IEEE Int. Conf. Compatibility, Power Electron. & Power Engr. (CPE-POWERENG)*, 2017.

[22] S. Kjaer, J. Pedersen, and F. Blaabjerg, "A review of single-phase grid-connected inverters for photovoltaic modules," *IEEE Trans. Ind. Appl.*, vol. 41, no. 5, pp. 1292-1306, Sept.-Oct. 2005.

[23] www.CDE.com// Type 381EL 1050C Ultra-Long Lift Snap-In, Aluminum

[24] M. Su, P. Pan, X. Long, Y. Sun, and J. Yang, "An active power-decoupling method for single-phase AC–DC converters," *IEEE Trans. Ind. Info.*, vol. 10, no. 1, pp. 461-468, Feb. 2014.

[25] H. Li, K. Zhang, H. Zhao, S. Fan, and J. Xiong, "Active power decoupling for high-Power single-phase PWM rectifiers," *IEEE Trans. Power Electron.*, vol. 28, no. 3, pp. 1308-1319, March 2013.

[26] A. Morsy and P. Enjeti, "Comparison of active power decoupling methods for high-power-density single-phase inverters using wide-bandgap FETs for google little box challenge," *IEEE J. Emerging Sel. Topics in Power Electron.*, vol. 4, no. 3, pp. 790-798, Sept. 2016.

[27] Y. Tang and F. Blaabjerg, "Power decoupling techniques for single-phase power electronics systems - An overview," *2015 IEEE Energy Conversion Congress and Exposition (ECCE)*, 2015, pp. 2541-2548.

[28] M. Chen, K. Afridi, and D. J. Perreault, "A multilevel energy buffer and voltage modulator for grid-interfaced microinverters," *IEEE Trans. Power Electron.*, vol. 30, no. 3, pp. 1203-1219, March 2015.

[29] Han H., Liu Y.L., and Sun Y. *et al.*: 'Single-phase current source converter with power decoupling capability using a series-connected active buffer', *IET Power Electron.*, 2015, vol. 8, no.5, pp. 700– 707.

[30] H. Watanabe, K. Kusaka, K. Furukawa, K. Orikawa, and J. Itoh, "DC to single-phase AC voltage source inverter with power decoupling circuit based on flying capacitor topology for PV system," in *Proc. IEEE Appl. Power Electron. Conf. Exposit. (APEC)*, 2016, pp. 1336-1343.

[31] X. Ma, B. Wang, F. Zhao, G. Qu, D. Gao, and Z Zhou, "A high power low ripple high dynamic performance DC power supply based on thyristor converter and active filter," in *Proc. IEEE 28th Annu. Conf. Ind. Electron. Soc.*, 2002, pp. 1238–1242.

[32] A. Kyritsis, N. Papanikolaou, and E. Tatakis, "A novel parallel active filter for current pulsation smoothing on single stage grid-connected AC-PV modules," *2007 European Conf. Power Electron. Appl.*, 2007, pp. 1-10.

[33] R. Wai and C. Lin, “Active low-frequency ripple control for clean-energy power-conditioning mechanism,” *IEEE Trans. Ind. Electron.*, vol. 57, no. 11, pp. 3780–3792, Nov. 2010.

[34] M. Chen, Z. Ye, Y. Chen, and D. Xu, "Zero-voltage-switching single-phase full-bridge inverter with active power decoupling," *IEEE Trans. Power Electron.*, vol. 36, no. 1, pp. 571-582, Jan. 2021,

[35] M. Vitorino, R.Wang, M. Correa, and D. Boroyevich, “Compensation of dc-link oscillation in single-phase-to-single-phase VSC/CSC and power density comparison,” *IEEE Trans. Ind. Appl.*, vol. 50, no. 3, pp. 2021–2028, May 2014.

[36] R. Wang, “High power density and high temperature converter design for transportation applications,” Ph.D. dissertation, Dept. Elect. Comput. Eng., Virginia Polytechnic Inst. State Univ., Blacksburg, VA, USA, 2012.

[37] H. Watanabe, J. Itoh, and Q. Roudier, "Single-phase power decoupling technique utilizing Hybrid method with passive and active power decoupling," *2018 IEEE Int. Power Electron. Appl. Conf. & Exposit. (PEAC)*, 2018, pp. 1-6.

[38] W. Yao, X. Wang, P. Loh, X. Zhang, and F. Blaabjerg, “Improved power decoupling scheme for a single-phase grid-connected differential inverter with realistic mismatch in storage capacitances,” *IEEE Trans. Power Electron.*, vol. 32, no. 1, pp. 186-199, Jan. 2017.

[39] L. Breazeale and R. Ayyanar, “A photovoltaic array transformer-less inverter with film capacitors and silicon carbide transistors,” *IEEE Trans. Power Electron.*, vol. 30, no. 3, pp. 1297-1305, March 2015.

[40] J. Zeng, T. Kim, and V. Winstead, “Decoupling control for single-phase photovoltaic inverter with film capacitor,” in *Proc. IEEE Energy Convers. Congress & Exposit.*, Cincinnati, OH, Oct., 2017, pp. 468-474.

[41] J. Zeng, M. Zhuo, T. Kim, V. Winstead, and L. Wu “Power pulsation decoupling for a two-stage single-phase photovoltaic inverter with film capacitor,” in *Proc. IEEE Energy Conversion Congress & Exposition* (*ECCE*). Cincinnati, OH, Oct., 2017, pp. 468-474.

[42] Z. Yang, J. Zeng, Q. Zhang, Z. Zhang, V. Winstead, and D. Yu, “A composite power decoupling method for a PV inverter with optimized energy buffer,” *IEEE Trans. Ind. Appl.*, vol. 57, no. 4, pp. 3877-3887, July-Aug. 2021.

[43] Z. Yang, J. Zeng, D. Yu, Q. Zhang, and Z. Zhang, “Two-stage power decoupling for a single-phase photovoltaic inverter by controlling the DC-link voltage ripple in the d-q frame,” in *Proc. IEEE Appl. Power Electron. Conf. Exposit. (APEC)*, New Orleans, LA, Mar. 2020, pp. 424-429.

[44] J. Zeng, J. Zhao, and V. Winstead “Modeling and control of a two-stage power decoupled photovoltaic inverter,” in *Proc. IEEE Energy Conversion Congress & Exposition* (*ECCE*), Portland, OR, Sept. 2018, pp. 991-997.

[45] Y. Ran, W. Wang, K. Liu, and H. Liu, “A power decoupling solution for improved Y-source single-phase grid-connected inverter,” *Electric Power Comp. Syst.*, vol. 46, no.11-12, pp.1387-1398, Nov. 2018

[46] J. Zeng, J. Ning, X. Du, T. Kim, Z. Yang, and V. Winstead, “A four-port DC-DC converter for a standalone wind and solar energy system,” *IEEE Trans. Ind. Appl.*, vol. 56, no. 1, pp. 446-454, Jan./Feb. 2020.

[47] H. Wang, G. Zhu, X. Fu, S. Ma, M. Xie, X. Li, and J. Jiang, “An AC side-active power decoupling modular for single phase power converter,” in *Proc. IEEE Energy Convers. Congress & Exposit.*, Montreal, QC, 2015, pp. 1743-1748.

[48] S. Li, W. Qi, S. Tan, and S. Hui, “Enhanced automatic-power-decoupling control method for single-phase AC-to-DC converters,” *IEEE Tran. Power Electron.*, vol. 33, no. 2, pp. 1816-1828, Feb. 2018.

[49] Y. Tang, Z. Qin, F. Blaabjerg, and P. Loh, “DQ reference frame modeling and control of single-phase active power decoupling circuits,” in *Proc. IEEE Appl. Power Electron. Conf. Expo.*, Charlotte, NC, 2015, pp. 2725-2732.

[50] R. Park, "Two-reaction theory of synchronous machines generalized method of analysis-part I," *Tran. American Institute of Electrical Engineers*, vol. 48, no. 3, pp. 716-727, July 1929.

[51] M. Gonzalez, V. Cardenas, and F. Pazos, "DQ transformation development for single-phase systems to compensate harmonic distortion and reactive power," *9th IEEE Int. Power Electron. Congress, 2004. CIEP 2004*, 2004, pp. 177-182.

[52] U. Miranda, L. Rolim, and M. Aredes, "A DQ Synchronous Reference Frame Current Control for Single-Phase Converters," *2005 IEEE 36th Power Electron. Spec. Conf.*, 2005, pp. 1377-1381.

[53] Y. Ohnuma and J. Itoh, “A novel single-phase buck PFC AC–DC converter with power decoupling capability using an active buffer,” *IEEE Trans. Ind. Appl.*, vol. 50, no. 3, pp. 1905-1914, May-June 2014.

[54] H. Sun, H. Wang, and W. Qi, “Automatic power decoupling controller of dependent power decoupling circuit for enhanced transient performance,” *IEEE Trans. Ind. Electron.*, vol. 66, no. 3, pp. 1820-1831, March 2019.

[55] S. Xu, R. Shao, L. Chang, and M. Mao, “Single-phase differential buck–boost inverter with pulse energy modulation and power decoupling control,” *IEEE J. Emerging Sel. Topics Power Electron.*, vol. 6, no. 4, pp. 2060-2072, Dec. 2018.

[56] Y. Sun, Y. Liu, M. Su, W. Xiong, and J. Yang, “Review of active power decoupling topologies in single-phase systems,” *IEEE Trans. Power Electron.*, vol. 31, no. 7, pp. 4778-4794, July 2016.

[57] C. Tang, L. Kao, Y. Chen, and S. Ou, “Dynamic power decoupling strategy for three-phase PV power systems under unbalanced grid voltages,” *IEEE Trans. Sustainable Energy*, vol. 10, no. 2, pp. 540-548, April 2019.

[58] A. Morsy and P. Enjeti, “Comparison of active power decoupling methods for high-power-density single-phase inverters using wide-bandgap FETs for Google little box challenge,” *IEEE J. Emerging Sel. Topics Power Electron.*, vol. 4, no. 3, pp. 790-798, Sept. 2016.

[59] J. Roy, Y. Xia, and R. Ayyanar, “High step-up transformerless inverter for AC module applications with active power decoupling,” *IEEE Trans. Ind. Electron.*, vol. 66, no. 5, pp. 3891-3901, May 2019.

[60] W. Yao, X. Wang, P. C. Loh, X. Zhang and F. Blaabjerg, “Improved power decoupling scheme for a single-phase grid-connected differential inverter with realistic mismatch in storage capacitances,” *IEEE Trans. Power Electron.*, vol. 32, no. 1, pp. 186-199, Jan. 2017.

[61] Y. Ran, W. Wang, K. Liu, and H. Liu, “A power decoupling solution for improved Y-source single-phase grid-connected inverter,” *Electric Power Components Syst.*, vol. 46, no.11-12, pp.1387-1398, Nov. 2018.

[62] D. Yu, J. Zeng, J. Zhao, and J. Ning, “A two-stage four-port inverter for renewable energy system integration,” in *Proc. IEEE Appl. Power Electron. Conf. Exposit.*, Anaheim, CA, Mar. 2019, pp. 3257-3262.

[63] S. Kjaer, J. Pedersen, and F. Blaabjerg, “A review of single-phase grid-connected inverters for photovoltaic modules,” *IEEE Trans. Ind. Appl.*, vol. 41, no. 5, pp. 1292-1306, Sept./Oct. 2005.

[64] Z. Shuai, H. Cheng, J. Xu, C. Shen, Y. Hong, and Y. Li, “A notch filter-based active damping control method for low-frequency oscillation suppression in train–network interaction systems,” *IEEE J. Emerging Sel. Topics Power Electron.*, vol. 7, no. 4, pp. 2417-2427, Dec. 2019.

Appendix

Optimized capacitance deduction for DC-link

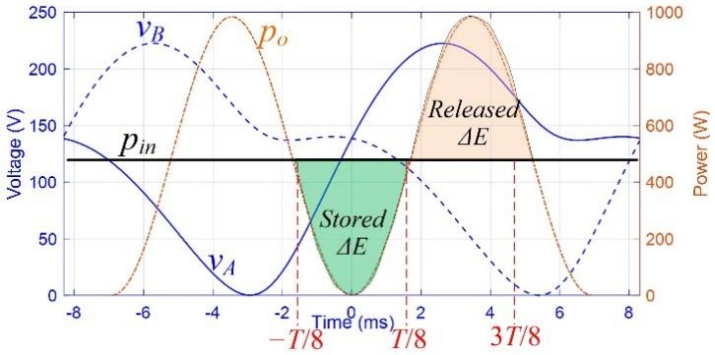

$$v_{AB}(t) = \pm\frac{\sqrt{2}V_o}{2}\sin(\omega t) + \sqrt{\frac{P}{2\omega C_d}\sin(2\omega t) - \frac{1}{2}V_o^2\sin^2(\omega t) + V_{co}^2} \tag{3}$$

Form -T/8 to T/8, pulsated energy absorbed by C_A and C_B are

$$\Delta E = \frac{1}{2}\cdot C_2\cdot\left[v_B^2\left(\frac{T}{4}\right) - v_B^2\left(\frac{-T}{4}\right) + v_A^2\left(\frac{T}{4}\right) - v_A^2\left(\frac{-T}{4}\right)\right] \tag{4}$$

The voltages at

$$v_A\left(-\frac{T}{4}\right) = \sqrt{\frac{-P_{ac}}{2\omega\cdot C_2} + V_{c0}^2 - \frac{V_o^2}{4}} - \frac{V_o}{2} \tag{5}$$

$$v_A\left(\frac{T}{4}\right) = \sqrt{\frac{P_{ac}}{2\omega\cdot C_2} + V_{c0}^2 - \frac{V_o^2}{4}} + \frac{V_o}{2} \tag{6}$$

$$v_B\left(-\frac{T}{4}\right) = \sqrt{\frac{-P_{ac}}{2\omega\cdot C_2} + V_{c0}^2 - \frac{V_o^2}{4}} + \frac{V_o}{2} \tag{7}$$

$$v_B\left(\frac{T}{4}\right) = \sqrt{\frac{P_{ac}}{2\omega\cdot C_2} + V_{c0}^2 - \frac{V_o^2}{4}} - \frac{V_o}{2} \tag{8}$$

Then energy change

$$\begin{aligned}\frac{2\Delta E}{C_2} &= \left(\sqrt{\frac{P_{ac}}{2\omega\cdot C_2}+V_{c0}^2-\frac{V_o^2}{4}}-\frac{V_o}{2}\right)^2-\left(\sqrt{\frac{-P_{ac}}{2\omega\cdot C_2}+V_{c0}^2-\frac{V_o^2}{4}}+\frac{V_o}{2}\right)^2 \\ &+\left(\sqrt{\frac{P_{ac}}{2\omega\cdot C_2}+V_{c0}^2-\frac{V_o^2}{4}}+\frac{V_o}{2}\right)^2-\left(\sqrt{\frac{-P_{ac}}{2\omega\cdot C_2}+V_{c0}^2-\frac{V_o^2}{4}}-\frac{V_o}{2}\right)^2 \\ &= 4V_{c0}^2\end{aligned} \tag{9}$$

During this period:

$$\Delta E=\int_{-\frac{T}{8}}^{\frac{T}{8}}\left(P_{ac}-P_{ac}\cdot\cos 2\omega t-P_{ac}\right)dt=\frac{2P_{ac}}{\omega} \tag{10}$$

Since the pulsated energy is absorbed by two capacitors, then

$$P_{ac}=\omega\cdot C_2\cdot V_{c0}^2 \tag{11}$$

Therefore, the AC side energy is determined by its voltage value at $t = nT$, then (1) can be

$$v_A(t)=\frac{1}{\sqrt{2}}\cdot\left[V_o\sin(\omega t)+\sqrt{V_{c0}^2\sin(2\omega t)-V_o^2\sin^2(\omega t)+2V_{c0}^2}\right] \tag{12}$$

$$d_{AB}=\sqrt{\frac{P_{ac}\cdot\sin(2\omega t)}{2\omega\cdot C_2\cdot V_{dc}^2}+\frac{V_{c0}^2}{V_{dc}^2}-d^2}\pm d \tag{13}$$

where $d = v_o/V_{dc}$. When $d_A(\omega t) = 0$,

$$\sqrt{\frac{P_{ac}\cdot\sin(2\omega t)}{2\omega\cdot C_2\cdot V_{dc}^2}+\frac{V_{c0}^2}{V_{dc}^2}-d^2}=d \tag{14}$$

$$\frac{P_{ac}\cdot\sin(2\omega t)}{2\omega\cdot C_2\cdot V_{dc}^2}+\frac{V_{c0}^2}{V_{dc}^2}=2d^2=\frac{V_o^2\cdot\sin^2(\omega t)}{V_{dc}^2} \tag{15}$$

Besides, d_A achieves the minimum value, $d_A'(\omega t) = 0$

$$\frac{d\left(d_A(t)\right)}{dt}=\frac{1}{2}\cdot\frac{\frac{P_{ac}\cdot\cos(2\omega t)}{2\omega\cdot C_2\cdot V_{dc}^2}\cdot 2\omega-2d\cdot d'}{\sqrt{\frac{P_{ac}\cdot\sin(2\omega t)}{2\omega\cdot C_2\cdot V_{dc}^2}+\frac{V_{c0}^2}{V_{dc}^2}-d^2}}-d' \\ =\frac{P_{ac}\cdot\cos(2\omega t)}{2C_2\cdot V_{dc}^2\cdot d}-2d'=0 \tag{16}$$

Then

$$2d\cdot d'=\frac{P_{ac}\cdot\cos(2\omega t)}{2C_2\cdot V_{dc}^2} \tag{17}$$

Because $d'=\frac{\omega V_0}{\sqrt{2}V_{dc}}\cdot\cos(\omega t)$ and

$$2d\cdot d'=2\cdot\frac{V_0}{\sqrt{2}V_{dc}}\sin(\omega t)\cdot\frac{\omega V_0}{\sqrt{2}V_{dc}}\cdot\cos(\omega t) \\ =\frac{1}{2}\cdot\frac{V_0^2\omega}{V_{dc}^2}\cdot\sin(2\omega t) \tag{18}$$

Then

$$\tan(2\omega t)=\frac{P_{ac}}{\omega\cdot C_2\cdot V_o^2} \tag{19}$$

and

$$\tan(2\omega t)=\frac{V_{c0}^2}{V_o^2}=m^2 \tag{20}$$

$$\sin(2\omega t)=\frac{P_{ac}}{\sqrt{P_{ac}^2+\left(\omega\cdot C_2\cdot V_o^2\right)^2}} \tag{21}$$

$$\cos(2\omega t) = \frac{\omega \cdot C_2 \cdot V_o^2}{\sqrt{P_{ac}^2 + \left(\omega \cdot C_2 \cdot V_o^2\right)^2}} \tag{22}$$

Since

$$\frac{V_{c0}^2 \cdot \sin(2\omega t)}{2 \cdot V_{dc}^2} + \frac{V_{c0}^2}{V_{dc}^2} = \frac{V_o^2 \cdot \sin^2(\omega t)}{V_{dc}^2} \tag{23}$$

$$\left[\frac{\sin(2\omega t)}{2} + 1\right] \cdot V_{c0}^2 = V_o^2 \cdot \frac{1 - \cos(2\omega t)}{2} \tag{24}$$

$$\left[\sin(2\omega t) + 2\right] \cdot \tan(2\omega t) = 1 - \cos(2\omega t) \tag{25}$$

then

$$\sin^2(2\omega t) + 2 \cdot \sin(2\omega t) = \cos(2\omega t) - \cos^2(2\omega t) \tag{26}$$

$$1 + 2 \cdot \sin(2\omega t) = \cos(2\omega t) = 1 - 2\sin^2(\omega t) \tag{27}$$

$$\tan(\omega t) = -2 \tag{28}$$

The ratio of V_{c0} and V_o can be derived:

$$\tan(2\omega t) = \frac{V_{c0}^2}{V_o^2} = m^2 = \frac{2\tan(\omega t)}{1 - \tan^2(\omega t)} = \frac{4}{3} \tag{29}$$

Therefore,

$$V_{c0} = \frac{2}{\sqrt{3}} V_o \tag{30}$$

The maximum decoupling power can be achieved, and its value is:

$$P_{ac,\max} = \frac{4}{3} \cdot \omega \cdot C_2 \cdot V_o^2 \tag{31}$$

The code for decoupling in d-q rotation frame

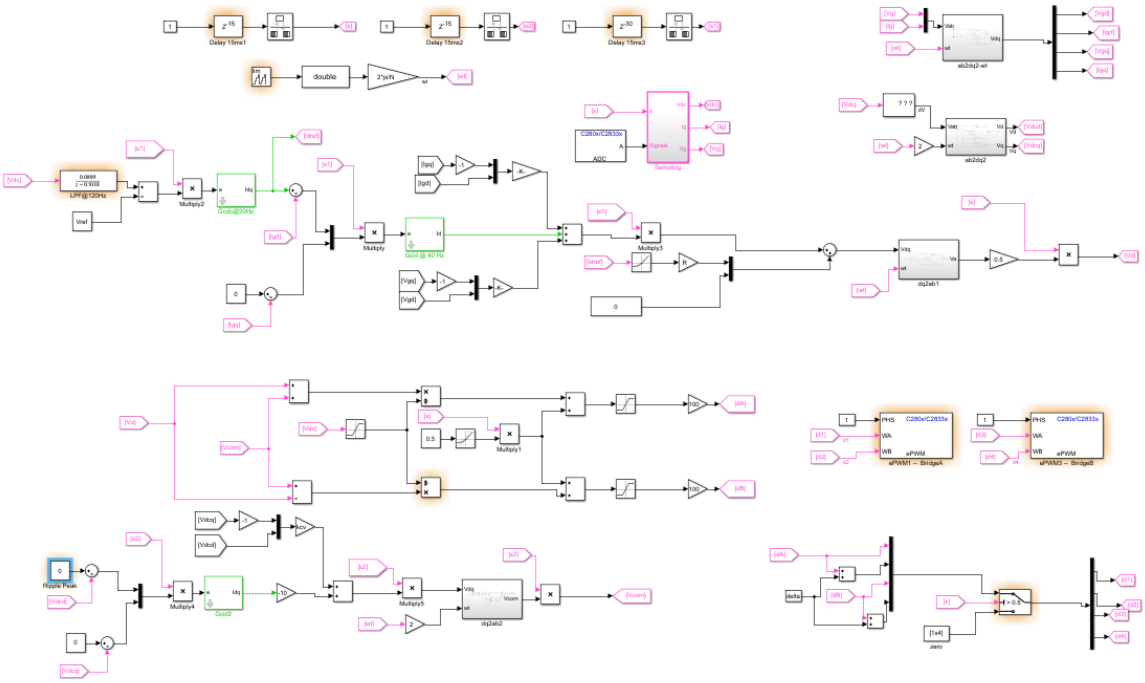

The code for composite power decoupling control

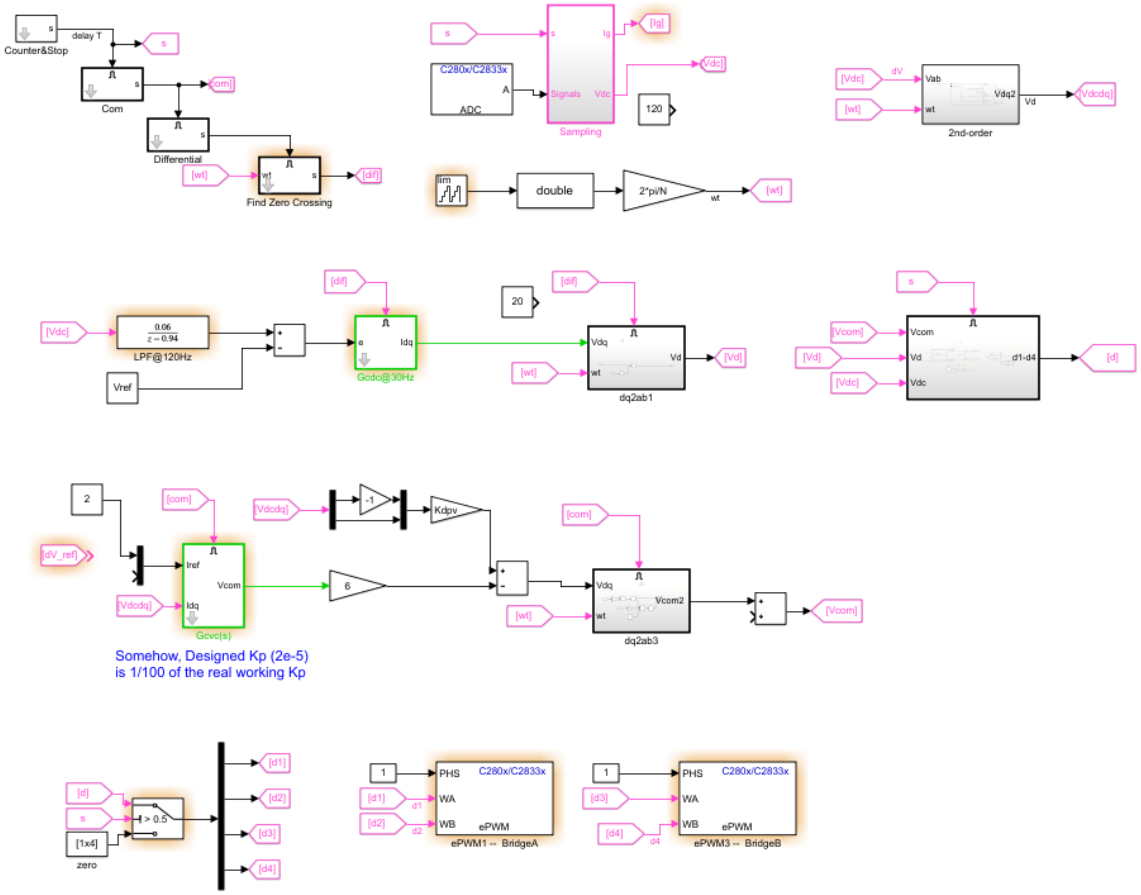

Organization of differential and common mode signals

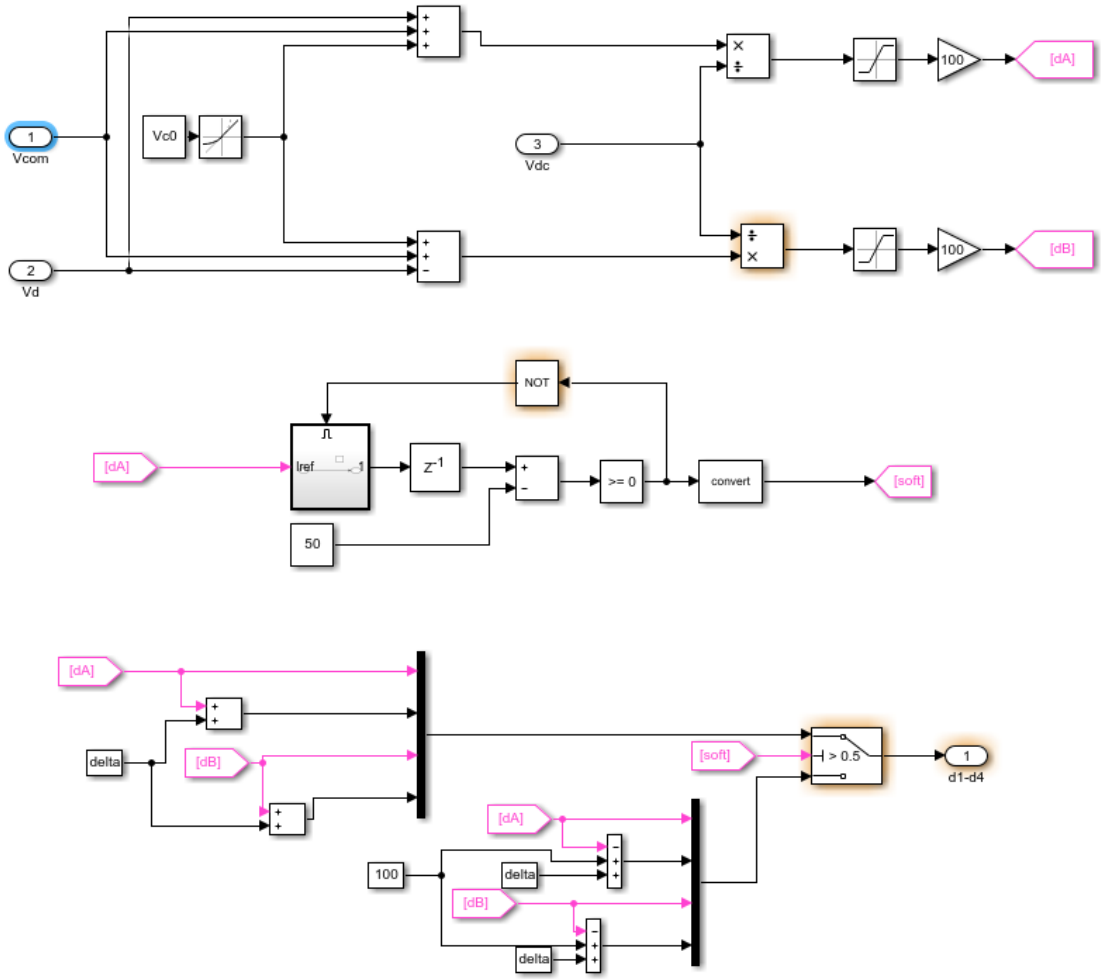

List of Publications

Refereed Journal Papers

[1] **Z. Yang**, J. Zeng, Q. Zhang, Z. Zhang, V. Winstead, and D. Yu, "A composite power decoupling method for a PV inverter with optimized energy buffer," *IEEE Trans. Ind. Appl.*, vol. 57, no. 4, pp. 3877-3887, July-Aug. 2021.

[2] **Z. Yang**, L. Wu, J. Zeng, Q. Ren, and Z. Liao, "A carrier-based discontinuous PWM for an 80 kW PV inverter with the reduction of the DC-link voltage ripple and common mode current," *IEEE Trans. Ind. Electron.*, (2^{nd} round review)

[3] **Z. Yang**, J. Zeng, Q. Ren, and L. Wu, "A semi discontinuous PWM method for suppression of the resonant current in a 48 kW grid-tied PV inverter," *IEEE Trans. Ind. Appl.*, (2^{nd} round review)

Refereed Conference Proceeding Papers

[1] **Z. Yang**, J. Zeng, Q. Ren, and L. Wu, "A semi-discontinuous PWM method for mitigating oscillation in a three-level grid-tied PV inverter," in *Proc. IEEE Energy Convers. Congr. Exposit. (ECCE)*, Vancouver, Canada, Oct. 2021, pp. 109-114.

[2] **Z. Yang**, J. Zeng, D. Yu, Q. Zhang, and Z. Zhang, "Two-stage power decoupling for a single-phase photovoltaic inverter by controlling the DC-link voltage ripple in the d-q frame," in *Proc. IEEE Appl. Power Electron. Conf. Exposit. (APEC)*, New Orleans, LA, Mar. 2020, pp. 424-429.